OPTICAL PROPERTIES AND DESIGN OF THE UNIVERSITY OF MANITOBA PROTON MICROPROBE

by

KOSAI ABDUL-RETHA

A THESIS

submitted to the Faculty of Graduate Studies
in partial fulfilment of the requirements
for the Degree of

MASTER OF SCIENCE

Department of Physics

University of Manitoba

WINNIPEG, Manitoba

ISBN 0-315-37267-2

OPTICAL PROPERTIES AND DESIGN OF THE UNIVERSITY OF MANITOBA PROTON MICROPROBE

BY

KOSAI ABDUL-RETHA

A thesis submitted to the Faculty of Graduate Studies of the University of Manitoba in partial fulfillment of the requirements of the degree of

MASTER OF SCIENCE

This thesis is dedicated to
my great and loving parents
and my wonderful wife.

"Do for your present life
as if you are living forever

and

Do for your later life
as if you are dying tomorrow."

(Imam Ali)

ABSTRACT

Since 1953 when the first device was built, the proton microprobe has become increasingly important as an analytical tool. This thesis describes work carried out to design the Manitoba Proton Microprobe. The Manitoba Microprobe is based on the "Russian quadruplet" lens system. The design goal was to achieve a minimum beam spot size using an iterative optimization procedure to arrive at a set of compromise values for several parameters. The optical characteristics of the "Russian quadruplet" lens configuration were investigated. A similar analysis was made on the pre-microprobe lens system; a magnetic doublet configuration. The microprobe system is optimized so that a spot diameter of 22.5 μm is achieved for the range of proton energies provided by the cyclotron. A brief review of some existing proton microprobes is given with the description of the advantage of the Manitoba Proton Microprobe System.

ACKNOWLEDGEMENTS

I would like to take this opportunity to express my sincere appreciation and thanks to the people who helped and supported me in this endeavour.

Thanks go to my supervisor, Professor J. S. C. McKee, Cyclotron Director, Physics Department, University of Manitoba, for his valuable advice during the course of this study, and for his constructive criticisms, suggestions and patience during the preparation of this manuscript.

I would also like to thank Dr. G. R. Smith, Physics Department, University of Manitoba, who has been an unfailing source of guidance from the very beginning of this work.

A special note of appreciation goes to Dr. K. Sharma and Dr. S. Oh of the Physics Department, University of Manitoba, for their provision of many valuable and helpful hints and also to Dr. M. S. A. L. Al-Ghazi for his moral support and encouragement.

Last, but not least, I would like to extend my utmost gratitude to my wife, Karen, for her helpfulness, encouragement and understanding during the course of this study.

TABLE OF CONTENTS

LIST OF FIGURES

LIST OF TABLES

INTRODUCTION

INTRODUCTION

A microprobe is a device which focuses a beam of ions into dimensions of a μm or less and is used for microanalysis in many fields of science. The electron microprobe, which focuses electrons, has developed into a precision instrument in recent years. Now, however, energetic ion microprobes are proving to have many advantages over the electron microprobe for analytical work. In particular, proton microprobes are beginning to play a major role in this field.

A proton microprobe is of value in many areas such as medicine, biology, metallurgy and geology. In the work presented in this text, a general, but qualitative description of the microprobe system is given. This comprises a summary of the beam optic theory involved in such systems and a survey of their configurations and overall performance. The University of Manitoba microprobe is based on the "Russian quadruplet" design of lens system (Dymnikov, 1965) which contains four magnetic quadrupole lenses.

In chapter (1), we explain the action of a microprobe facility in general and the rules governing its performances and characteristics. Various techniques for microbeam production are also reviewed. A comparison with the classical electron microprobe and the advantages of the proton microprobe over such systems are given in detail. A simple but adequate representation of a magnetic quadrupole and the field distribution inside the aperture is also presented. Chapter (2)

contains a historical review of proton microprobe development and its progress over the years. This is illustrated by a review of the major facilities which utilize beams with energies in the range from 1→6 Mev from tandem and single-ended Van de Graaff accelerators as well as facilities which use beams extracted from higher energy cyclotrons. Through this review, the capability of different lens configurations and arrangements in producing the microprobe image is identified through a review of available and reported data. At the end of this chapter, we give the characteristics of our adopted design and the many advantages this system may offer.

The theoretical aspects of such devices are of importance. The matrix method is one of the most common techniques applied by scientists to beam transport system analysis today. We have employed in our study two computer codes which utilize this particular method for beam optic calculations. The method is described and derived from the equations of motion of the beam in chapter (3). The derivation is initially made by using a transfer matrix representation to first order for each system element. Matrix multiplication is carried out in that fashion for the "Russian quadruplet" lens configuration which has been chosen for our microprobe facility. The main lens parameters are then derived from the elements of the final matrix. The method for expanding the transfer matrix from the first order to include coefficients of up to and including the third order is then presented in a simple form.

In order to understand the relationships between the many lens and beam parameters and the influence of such relationships on the microbeam spot size we have attempted to assess the effects of varying one parameter or more at a time and record the change in other factors in chapter (4). The effects of the separation distance between neighboring quadrupoles, object distance, image distance, beam energy and divergence angles, etc., on the spot size are examined. Calculations involving aberration coefficients to third order are essential in any lens system analysis since the contribution of such aberrations is very large and destructive to the image quality and size. The effects of the main aberration coefficients on the lens and the beam parameters were determined under various assumptions such as: a) fringing field effects are ignored and b) two particular kinds of fringing field functions are considered. Graphic figures of the distribution of protons at the image plane considering up to third order effects were obtained from a Monte Carlo simulation technique. These figures have displayed the contributions of the chromatic and the spherical aberrations to the spot size for different values of energy spread and beam divergence angles.

From the results of the analysis and calculations of chapter (4), optimization processes were followed for the purpose of realizing the best configuration for our design. The calculations also provided the acceptable initial beam parameters for the microprobe system so that an optimum image size could be obtained. The final design of our microprobe facility is reported in chapter (5). Further, details about

the tests performed on the lens elements, the construction procedure for these elements and the final assembly of the system are given.

In the last chapter, we reach a number of conclusions and make suggestions which result from this study.

CHAPTER 1

ROLE AND FUNCTION OF THE PROTON MICROPROBE

CHAPTER 1

ROLE AND FUNCTION OF THE PROTON MICROPROBE

1.1 Historical review of the microprobe

Electron microprobes have been in existence for the last fifty years and are used for x-ray analysis in various branches of science. It was not until the end of the 1960's that physicists started to think of possible ways to reduce the large background effects associated with an electron microprobe. By combining the enormous knowledge of electron optics and the accelerator related ion optics[1], scientists made the first step towards the development of a new and more sophisticated analytical tool, the proton microprobe.

Using proton microbeams rather than electron microbeams has many advantages. The total bremsstrahlung background observed in electron systems is reduced in the proton microprobe since it is proportional to the square of m_e/m_p [2,3]. The proton microprobe allows us to detect certain undetectable trace elements (e.g. rare earth) at the ppm level[4] which cannot be detected by the electron microprobe. This fact has been demonstrated on various occasions. An additional advantage of proton microbeams is their low multiple scattering of protons compared to electron microbeams. This is due to their higher energy[1] and mass. Our system will utilize a new analytical technique of beam transmission

through a very thin target to produce a monoenergetic x-ray emission.

The first ion microbeam ever produced was in 1953 by Zirkle and Bloom[5] using the collimation method. However, Cookson et al. had the privilege of building the first focusing proton microprobe at A.E.R.E., Harwell in 1969[5]. Since then the number of existing microprobes has grown exponentially. Most of these systems focus the proton beam to a few micrometers in spot size and such resolutions are sufficient for most applications of the instrument. However, an interest in examining samples of dimensions down to a micron in size has established the need for smaller beam sizes; a fact which has encouraged system designers to search for methods of reducing the contribution of aberrations to beam spot size. Recently, Microscope Associates, Inc. have reported their achievement in producing a 0.5x0.5 μm^2 spot at 1.2 MeV proton energy from an achromatic magnetic doublet[6].

1.2 Proton induced x-ray emission analysis with a microprobe

It has been reported[7] that proton induced x-ray emission (PIXE) was first used as an analytical technique for trace elements in 1968. Since that time the tool has been widely accepted as a powerful analytical method for detecting multiple elements simultaneously with high sensitivity in many instances to ppb. This high sensitivity has been reached because of the development of high resolution x-ray detectors. Another advantage of using PIXE for trace element analysis is its characteristic of being non-destructive to the analyzed sample.

PIXE is produced by an atomic process in which there is an energy dependent probability that a proton at high energy will knock out an inner-shell electron from atoms in the target. When electrons from higher energy levels move to fill the gap created by the ejected electron, an x-ray quantum will be emitted (figure 1.1). The energy of this emitted x-ray is characteristic of the target atom. By using high resolution solid-state detectors, which can detect a wide range of x-rays as well as resolving various energies of x-rays efficiently, we can obtain information about the elements and their concentrations in the target under consideration.

There are however some difficulties inherent with the PIXE method. The detection limits are determined by x-ray production cross sections and the continuous background radiation which results from the interaction of the proton beam with the sample[8]. Since the K x-ray production cross-section is a function of incident particle energy, the study of such rays should be constructed at that proton energy for which the yield is maximum[9].

With PIXE, samples are irradiated with proton beams of size 2 mm in diameter and results obtained for relatively large areas of the sample. These results are accurate enough to give the elemental composition of a sample with no reference to the elemental distribution within the sample. The concept of the microprobe is to reduce the beam size to the μm level so that it becomes smaller than the size of a plant or animal tissue cell. Once this is achieved, we will have a more

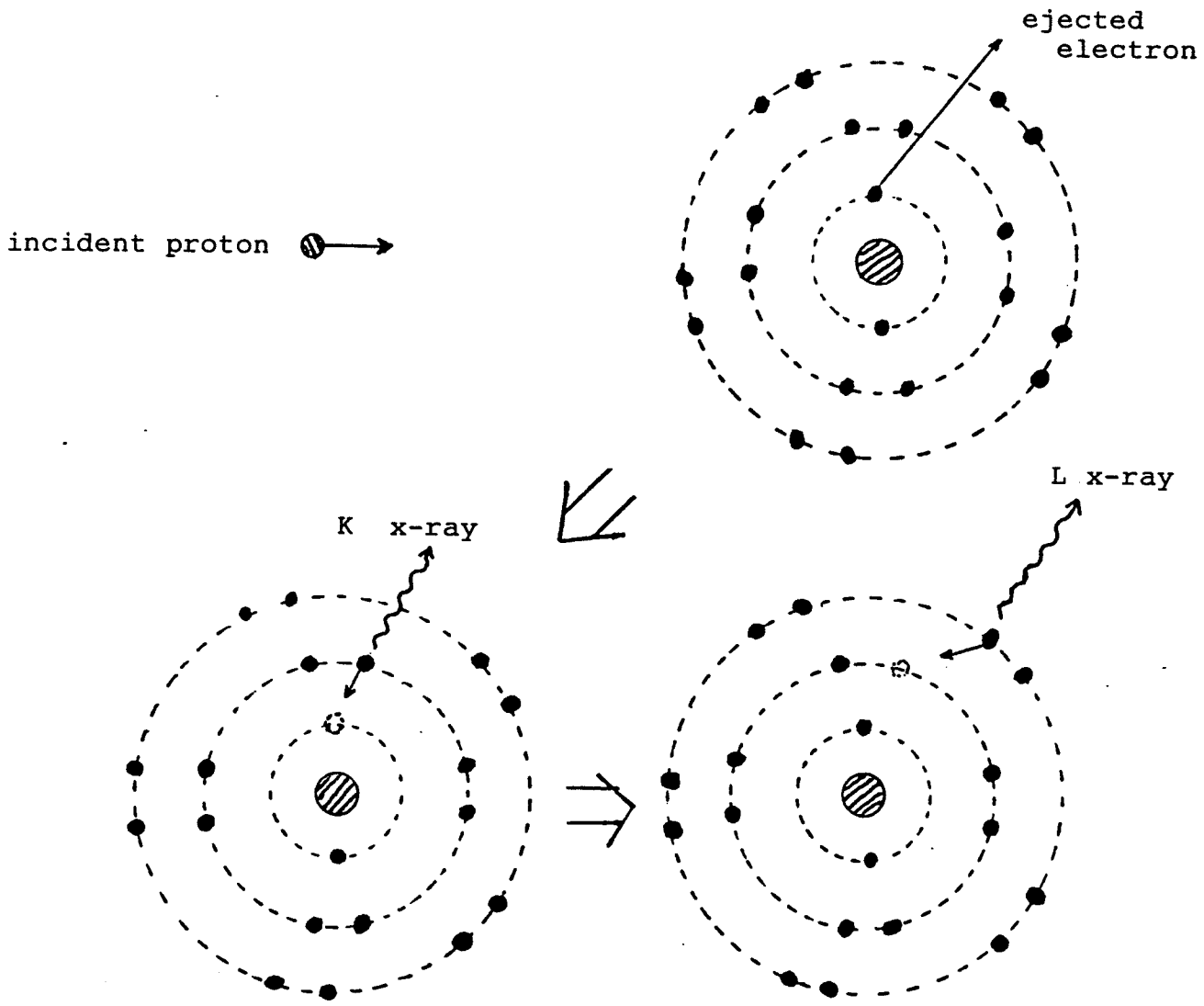

Figure 1.1 Schematic diagram of the process of Proton Induced X-Ray Emission (PIXE) to produce the characteristic K and L x-rays.

powerful tool for analysis.

Information may be obtained by scanning the beam in order to survey the chemical composition of the cell itself. This valuable, detailed information on trace elements, which includes their concentration and distribution within microscopic volumes of the sample, is of great importance in advancing several areas of science.

1.3 The function and variety of proton microprobes

As described above, the objective of building a proton microprobe is to find a means to focus a proton beam to a few micrometers or even a fraction of a micrometer in size. Two available techniques can be employed to achieve such a small beam dimension; collimation or focusing the particle beams.

1.3.1 Collimation microprobes

This is the simplest of the two techniques. It does not employ any type of lens to produce fine beams. The beam dimensions are defined by a collimating diaphragm and depend upon the degree of beam scattering from the collimating edge. As previously mentioned, the first microbeam was produced using this method seventeen years before the first focusing microprobe was built at Harwell. This microbeam was satisfactory for the purpose at the time, which was to study the effect of radiation on animal cells. There are several drawbacks which set limitations on the

use of a collimated microbeam. The transmitted current of the collimated beam is proportional to the area of the collimating aperture. The scattering of particles from the slit edge adds a halo to the beam size which is proportional to the circumference of the slit[5]. Separate studies have been done to improve the performance of the slit by studying the effect of slit thickness and shape on the beam scattering. This topic will be discussed in chapter (5). Since the collimation microprobe employs no focusing elements, the angular divergence of the beam after passing through the collimating slit should be very small so as to minimize the beam spreading when it hits the target[10]. This can be made possible by using a lens system prior to the collimator; however, Liouville's theorem, which states that the emittance of a beam with fixed energy is a constant, implies that any reduction in the divergence of the beam at the object position will result in an increase in its dimensions at the image position and therefore creates a large reduction in the beam intensity after passing through the collimator.

To avoid low beam intensity while simultaneously maintaining a narrow beam, the target has to be placed very close to the collimation system. Again this presents another problem, namely that of higher background radiation from the collimator material. It has also been found that practically, it is difficult to construct a microcollimator with a diameter less than 10 μm from material thick enough to stop the incoming beam[10].

1.3.2 Focusing microprobes

This method is far superior to the above technique and has been employed by most laboratories around the globe. Most of the problems associated with the collimating technique may be overcome by this method. Basically, it requires a focusing system to receive the beam emerging from an object slit and demagnify it to a few μm's or smaller. This focusing system may be designed to focus in one or two steps. There are several problems which arise from using a two-step focusing system. Because of the very long two-step system, it is very difficult to achieve stability and precision for such small beam sizes. Moreover, the residual gas scattering will increase the beam emittance and the aberrations are higher than in single-step focusing[8].

The focusing system may be constructed using electrostatic or magnetostatic lenses. Electrostatic lenses can be used successfully with low energy beams in the KeV range, however, with beams of higher energies in the MeV range (the lowest range used for proton microprobe analysis) it becomes difficult to employ such a lens system. Solenoids are commonly used in most electron microprobes today, as is the case with low energy ion probes. There are, however, practical and economic limitations to the use of such lenses for high energy proton microprobes. The other alternative is to consider the strong focusing quadrupole magnet. This type of magnet can provide the desired focusing with fields of moderate strength. The majority of the focused proton

microprobe laboratories use quadrupole lenses.

The principle of focusing by a quadrupole magnet is well documented and studies have continued for many decades to improve the pole tip shape resulting in a more homogeneous magnetic field distribution containing fewer field harmonics. Quadrupole magnets have four identical poles, alternately N and S, as shown schematically in figure 1.2.

As can be seen from the orientations in figure 1.2, the final effect of the magnet is focusing in the xz-plane and defocusing in the yz-plane. The field is zero at the centre of the aperture and increases linearly as we move away from the centre in a particular direction. Typically, this field variation should provide a constant field gradient. However, this may not be the case everywhere within the aperture due to the effects of pole shape on the field distribution. Since a quadrupole magnet focuses in one plane and defocuses in the other, two such magnets are required to obtain focusing of the beam in both planes.

Magnetic quadrupole multiplets are not the only type of lens employed for probe-forming systems. At Los Alamos[11], they are using a superconducting solenoid to obtain beam sizes of 5 μm in diameter. The only limitation imposed on this lens is due to the chromatic aberrations. Although this type of superconducting solenoidal lens

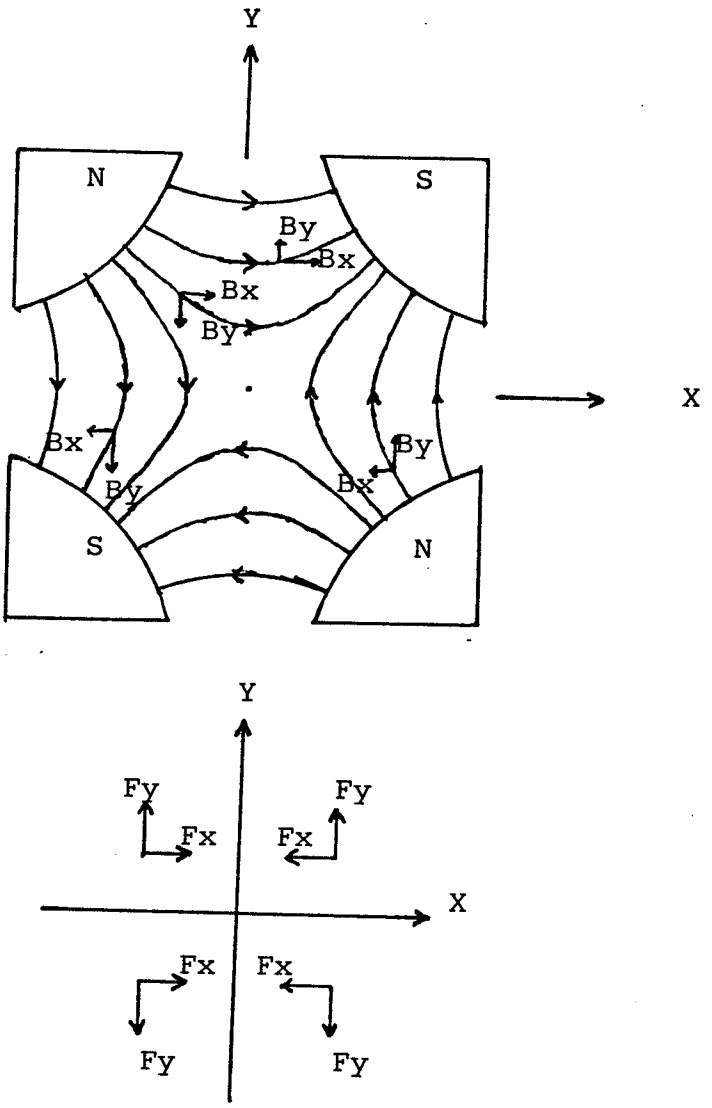

Figure 1.2 Schematic diagram of the quadrupole magnet.
a) the field orientations and components, and,
b) the resultant force orientations, within the aperture.

represents a very interesting development in this field, it still cannot be taken as a replacement for the magnetic quadrupole multiplet.

CHAPTER 2

REVIEW OF SOME OF THE EXISTING RELATED FACILITIES AND THE CHARACTERISTICS OF THE MANITOBA PROTON MICROPROBE

CHAPTER 2

REVIEW OF SOME OF THE EXISTING RELATED FACILITIES AND THE CHARACTERISTICS OF THE MANITOBA PROTON MICROPROBE

According to Legge[13] 1982, there are about 27 focused proton microprobe systems currently in use. A majority of these facilities focus beams by means of combinations of quadrupole magnets. The various possible combinations will be described when we review some of the reported facilities. In addition to the focused proton microprobes, there are several collimation proton microprobe systems in operation[12]. Our interest is in focusing proton microprobes. Only references pertaining to the collimation type will be given here. At Birmingham University, a beam from a 3 MeV dynamitron is collimated to 20-1000 μm in diameter and is mainly used for material science. A 2 MeV beam from a Van de Graaff accelerator is collimated to 50-500 μm at Delaware University, Bartol. At Brooklyn College, N.Y. and Queen's University, Kingston, beams from 4 MeV Van de Graaff accelerators are successfully collimated to 20 μm and 10 μm respectively. There are several other collimation proton microprobes which have been reported[5] which may or may not still be on-line today.

2.1 Oxford Proton Microprobe

In this system, which has been operational since 1978[5], they have

adopted the coupled triplet CDC* where the first and the second quadrupole lenses are coupled together to have the same excitation. Although this configuration suffers from relatively high intrinsic and parasitic aberration coefficients[4], the xz- and yz- demagnifications of 66 and 15 respectively, provide a 1x1 μm^2 spot size with an 80 $pA/\mu m^2$ current density[10]. An adjustable stainless steel object aperture is located 5.786 m from the first quadupole. Due to this relatively long object distance, collimator slits are used to control the beam envelope in order to match the lens aperture. The quadrupole magnets are composed of Swedish iron[12] and are individually adjustable in all directions. Each quadrupole has an effective length of 21.4 cm and has an aperture with a radius of 1.5 cm. The space between the adjacent quadrupoles is 4.6 cm and the image distance is 16 cm for the above given spot size[4]. This facility is used to focus a proton beam from a 4 MeV EN tandem Van de Graaff accelerator.

2.2 Heidelberg Proton Microprobe

This facility was built in 1976[5] and may be one of the shortest systems (2.1 m) capable of focusing a proton beam from a 6 MeV EN tandem Van de Graaff accelerator to approximately a 2x2 μm^2 spot size[13] and a current density of 20 $pA/\mu m^2$. This is achieved by a short, but

---

* The symbols of the combinations in this text are used to refer to the lens action in the xz-plane. The letters C and D indicate the converging and diverging elements respectively. Clearly it implies the opposite action in the yz-plane.

powerful, high gradient (400 T/m), magnetic quadrupole doublet of CD configuration[14]. The high magnetic field gradient was obtained by choosing a very narrow quadrupole aperture, 2.5 mm in radius[8], in addition to positioning the wound coil very close (4 mm) to the aperture. The achieved xz- and yz-demagnifications are 4 and 23 respectively at approximately a 10 cm image distance. The aberrations are low. Moreover, for the magnet material, the choice of 50% Fe and 50% Co alloy with a saturation of 2.3 T, together with the material's special treatment were essential for obtaining the good performance. The system employed two sets of collimator slits[15]. They are of an ingenious design due to Nobiling and are used to adjust the area as well as the divergence of the beam. The first collimator set, which is used to define the object slit, has the front edges made of tungsten carbide. Such material allows for very smooth surfaces and can be attained with approximately a 0.05 μm roughness[8] which has the effect of greatly reducing the slit scattering. The second collimator set is located one meter downstream from the first one to independently adjust the beam divergences in the xz- and yz-planes to define the acceptance of the lens. The effective length of each quadrupole singlet is approximately 4.27 cm and the separation distance within the doublet is 4 cm.

2.3 Harwell Proton Microprobe

As has been reported earlier, this is the oldest (1969) high energy focusing proton microprobe ever built. The "Russian quadruplet" of antisymmetric CDCD configuration is utilized for beam focusing to

obtain an orthomorphic image i.e. an image with the same dimension in the x and y directions, for an object from a circular collimating aperture[8]. This feature of equal demagnification in the xz- and yz-planes is similar to that of a cylindrical lens which makes this design configuration very popular and attractive[12]. The object was initially defined by a collimator made of simply drilled holes which produced large slit edge scattering thereby adding to the halo around the beam. With the existence of another collimator at approximately 3 m from the object slit, the halo was reduced to 4-5% of the beam intensity. This high proportion of the beam going to the halo was however of concern and was subjected to intensive investigations which lead to the replacement of the drilled apertures with slits thus achieving a substantial improvement in the image quality[3]. All quadrupoles have the same dimensions, though the excitation value for the first and the last differ from that of the second and the third. Each quadrupole has an effective length of 21.15 cm and is made up of Swedish iron. The aperture radius is equal to 1.92 cm and the distance between adjacent quadrupoles is approximately 4.5 cm. This arrangement has a demagnification of 5.6 at an object distance of 3.5 m and an image distance of 21 cm. Therefore an image size of 4x4 μm^2 is routinely accomplished at a current density of about 30 $pA/\mu m^2$ from a 3 MeV Van de Graaff accelerator. The intrinsic aberration has an effect of less than 1 μm on the spot size. In order to reduce the parasitic aberrations, four accurately constructed quadrupole lenses, which can be easily adjusted with respect to each other rotationally, were designed and built.

This facility is used for applications which require a high current density. For this purpose only three of the four quadrupoles are used in a DCD configuration with the second quadrupole lens non-excited and the first one connected as a diverging lens. This combination, which has demagnification of 8.8 and 18.9 in the xz- and yz-planes respectively, can produce a very bright spot with a current density of 150 $pA/\mu m^2$ and some limitations on the spot size due to chromatic aberration[5].

2.4 Zurich Proton Microprobe

This is one of the earliest facilities and was built in 1974. The microprobe uses a proton beam from a 6 MeV tandem accelerator[5]. It represents quite a different assembly to the others described earlier. The demagnification is accomplished by employing the two-step focusing technique mentioned in section (1.3.2) of chapter (1). The microprobe comprises two magnetic quadrupole doublet lenses (CDCD configuration) separated by a large drift distance. As a result of this configuration, the Zurich microprobe may be the longest of all existing facilities today (17.5 m). This arrangement has a high demagnification of 100 in both the xz- and yz-planes[5,10] and therefore allows large separation object slits. Such a wide aperture for the collimator has the advantage of limiting the contribution of the slit edge scattering to the halo around the focused spot[8].

The object is defined by a first collimator to 1x1 mm^2 and is focused by the first doublet lens whose quadrupoles have an effective length of about 25.4 cm each and a bore radius of 2.55 cm. This beam is brought into an intermediate focus as a result of the large drift length to the second doublet lens. Another collimator is placed between the two doublets to limit the beam solid angle in order to match the acceptance of the second doublet. The quadrupoles of the second doublet have an effective length of 23.5 cm each and a bore radius similar to the first set (i.e. 2.55 cm). In spite of the high demagnification, a desired resolution of 10x10 μm^2 could not be achieved due to the high intrinsic and parasitic aberrations which increase dramatically in such configurations[8]. At an image distance of 48 cm, the achieved spot size is 11x26 μm^2 with a current density of 1-2 $pA/\mu m^2$. This low current density is a consequence of the second limiting collimator. In addition, there are some other drawbacks associated with this arrangement such as low system stability and residual gas scattering. Furthermore, there is a measurable effect due to the earth's magnetic field which tends to divert the proton beam from its direction.

2.5 Other conventional proton microprobes

In this section, we will briefly review some other available facilities because of their similarity to the focusing systems described above or because of limited literature being available.

At Karlsruhe, a system similar to Heidelberg i.e. a CD configuration, was developed in 1977 for their 3 MeV Van de Graaff accelerator. A larger spacing between the magnets was used to improve the current density. By this method, 120 pA/μm^2 was achieved in a 2.5x2.5 μm^2 spot size. With an effective length of each quadrupole being 10 cm and a bore radius of 2.5 cm demagnification of 2.4 and 39 in the xz- and yz-planes was provided[10], as well as a very low halo-to-beam ratio[8] of 1:2500. At Sandia laboratories, a doublet system is used with their 5 MeV tandem accelerator and has achieved almost the same performance as at Heidelberg[10]. Very strong focusing quadrupoles, which have a bore radius of 1.69 mm and a lens length of 6 cm[1], are used in the doublet. A system similar to the Zurich proton microprobe was constructed at UCLA in 1974[5,12]. This facility has a total length of 8.1 m, which is approximately half that of the Zurich system, and can produce a resolution of 8x8 μm^2 with a 1 pA/μm^2 current density[10]. The Bochum proton microprobe originally employed a closely spaced quadruplet, as at Harwell, with non-symmetrical excitations. The best spot size achieved here was 40x60 μm^2 due to large aberrations and poor design[5]. Later, the lens configuration was modified and a spot size of approximately 2x2 μm^2 with current density of 20 pA/μm^2 was achieved[16,17]. Other facilities which use magnetic quadruplets and yield similar performances are at Manchester, Surrey and Namur[5]. In 1978, another "Russian quadruplet" was installed at Melbourne to focus a beam of 5 MeV which initially comprised lenses with a 2.5 cm bore radius[1]. This arrangement produced a 10x10 μm^2 spot and a current density of 1 nA/μm^2. Recently, it was rebuilt with a lens of bore

radius equal to 6.35 mm which improved the spot dimensions to 1.5x1.5 μm^2 at a current density of 150 $pA/\mu m^2$. Improvement in this proton microprobe performance was recently reported[6]. By means of an achromatic quadrupole doublet lens, a spot size of 0.5x0.5 μm^2 was achieved at Microscope Associates, Inc. This system eliminates chromatic aberrations; however the image quality and the focusing performance were found to be limited by other types of aberration. Each quadrupole has a length of 6 cm and the lens separation is 7 cm. At an object distance of 3.6 m and an image distance of 10 cm, a demagnification of 70.5 and 10.2 in the xz- and yz-planes respectively are achieved for a proton beam from a 1.2 MeV Van de Graaff accelerator.

2.6 Proton microprobes for cyclotron beams

There are few facilities in operation today which focus beams extracted from cyclotrons. This is a new and very interesting dimension for proton microprobe development and progress. A brief summary on the performance of these microprobes is given here.

At Eindhoven University a magnetic quadruplet was installed to focus a proton beam of 3.5 MeV to a 24x25 μm^2 spot[18] through an object-to-image length of 8 m. The demagnification of this system is 50 in both planes provided by the quadruplet with a bore radius of 2.5 cm.

The IMS microprobe at Tokyo has achieved a 60x60 μm^2 spot from a 25 MeV beam[19].

A doublet system with a length of 1.9 m and demagnifications of 4.5 and 25 in the xz- and yz-planes respectively was assembled at Vrije University, Amsterdam in 1981. By adopting Heidelberg's concept, they have built a high field gradient quadrupole system with an aperture equal to 4 mm in order to focus a beam of up to 8 MeV to a spot size of 3x8 μm^2. The quadrupole pole pieces are made up of 50% iron and 50% cobalt and the yokes are manufactured from cast iron[19]. The system is composed of two pairs of slits made out of stainless steel and shaped according to the Nobiling design in order to reduce slit edge scattering.

Another magnetic doublet was installed at the Hamburg isochronous cyclotron. Through a 10 m long system and demagnifications of 3.3 and 12.5 in the xz- and yz-planes respectively, a 40x40 μm^2 spot is achievable for beams from 10 to 30 MeV. The doublet has a bore radius of 2.5 cm. This facility started operating in 1981[20]. A scanning magnet is used after the quadrupole doublet to control the beam deflection.

2.7 The concept and the advantage of the Manitoba Proton Microprobe

For more than ten years after Harwell produced the first focused proton microbeams, Van de Graaff accelerators (2-6 MeV) were the favorite sources for such purposes. The claim was that the above energy range is the optimum for x-ray studies. Higher energies were thought to introduce a high background rate[10] due to bremsstrahlung radiation, and compton scattering in the detector caused by γ-radiation from the target. However, beams of such relatively low energies (2-6 MeV) have low x-ray production cross-sections for K x-rays and will result in an overlapping of L and K x-rays in the spectra[10]. Beams of higher energies such as in the range of 20-50 MeV produce good yields of K x-rays from medium and high Z elements. Hence, simultaneous analysis of multi-element samples with Z>10 becomes possible even for elements which are adjacent to each other in the periodic table[21,22]. Furthermore, the K x-rays experience less attenuation than L x-rays. Beam energies of higher than 6 MeV, however, are generally produced by cyclotrons, the beam optics of which are not ideal for microprobe applications[12]. At the beginning of this decade, scientists began investigating the possibility of cyclotron beam improvements in order to achieve high quality microbeams. We have shown in section (2.6) that this effort was very successful and there are several such facilities already operational. The idea of developing a micro-PIXE facility at the University of Manitoba Spiral Ridge Cyclotron with all the advantages that are stated above provided by a higher energy range of proton beams,

was subject to very intensive investigations. The design structure and the detailed analysis of the beam optic parameters are given in the following chapters.

CHAPTER 3

THEORETICAL ASPECTS OF THE MANITOBA PROTON MICORPROBE

CHAPTER 3

THEORETICAL ASPECTS OF THE MANITOBA PROTON MICROPROBE

An antisymmetric quadruplet with a rectangular shaped field distribution along the beam axis was adopted for the Manitoba Proton Microprobe. This CDCD (in xz-plane) and DCDC (in yz-plane) configuration, is commonly referred to as a "Russian quadruplet" named after the Leningrad group who first studied the Gaussian properties of the antisymmetric quadruplet lens[23]. The results of these studies were collected and published by Dymnikov et al. in 1965[24]. The justification of this choice is straightforward.

Although other design structures e.g. the magnetic doublet and the triplet, were used successfully in other facilities, as described in chapter (2), due to the relatively high energy proton beams of the Manitoba Cyclotron and disadvantages associated with those structures we utilized the quadruplet lens. The doublet has a smaller degree of freedom than the triplet and the quadruplet and any variation of one parameter in one plane leads to a significant variation of the parameters in the other[23,25].

Another disadvantage of the doublet is that in order to obtain an orthomorphic image, it required a very difficult and non-practical arrangement. In this system the collimator slit is designed in such a

way as to produce an object with nonsymmetrical dimensions corresponding to the demagnification powers of the lens in the xz- and yz-planes. This means that the beam will enter the quadrupole magnets of the lens at different radii for the xz-plane than the yz-plane. The admixture of higher order harmonic components to the field depends upon radius inside the aperture of the quadrupole. The effect on the final image is thus assymmetric and increases the complication of the calculations for transporting the beam through the quadrupole.

The symmetrical triplet structure has the advantage of independent control over the focusing action in the two xz- and yz-planes. It does not have the above mentioned disadvantages, however, it has another sort of problem which the doublet suffers from too. Since the protons are moving at high energies and the beam usually has an initial divergence angle, a large portion of the beam will be lost unless we choose a large aperture lens[25]. This choise places more stringent requirements on maintaining the required field gradient within the aperture.

The best alternative to overcome most of these problems, as well as to introduce some extra advantages, is to use a system of four quadrupoles. Among the advantages are the high focusing power and the better beam quality due to correction of some types of aberrations[24]. The quadruplet also provides the stability conditions which are required to avoid particle excursions during beam transportation inside the system. This stability is due to the identical structure of all

quadrupoles[25].

Various combinations of converging and diverging lenses can be employed to assemble a system of quadrupoles. Their optical properties, which were investigated extensively by Grime and Watt and presented in graphical form[10], support our choice of the CDCD configuration where the first and fourth quadrupoles are connected to one DC power supply and the second and third to the other. This configuration introduces small second order chromatic aberration coefficients compared to most of the other combinations. Further this lens configuration effects the beam in both transverse planes equally, to produce an orthomorphous image.

3.1 First order matrix method

In order to obtain the optical parameters for this combination of quadrupole lenses and to show its symmetrical effect on the beam for both transverse (xz and yz) planes we have to solve the beam equations of motion and to derive the transfer matrices for these planes.

For simplicity, first order terms in the solutions of these equations of motion were used to derive the first order transfer matrix of the quadruplet lens system. Second and third order terms can be applied to develop the third order transfer matrix of the system in a similar fashion.

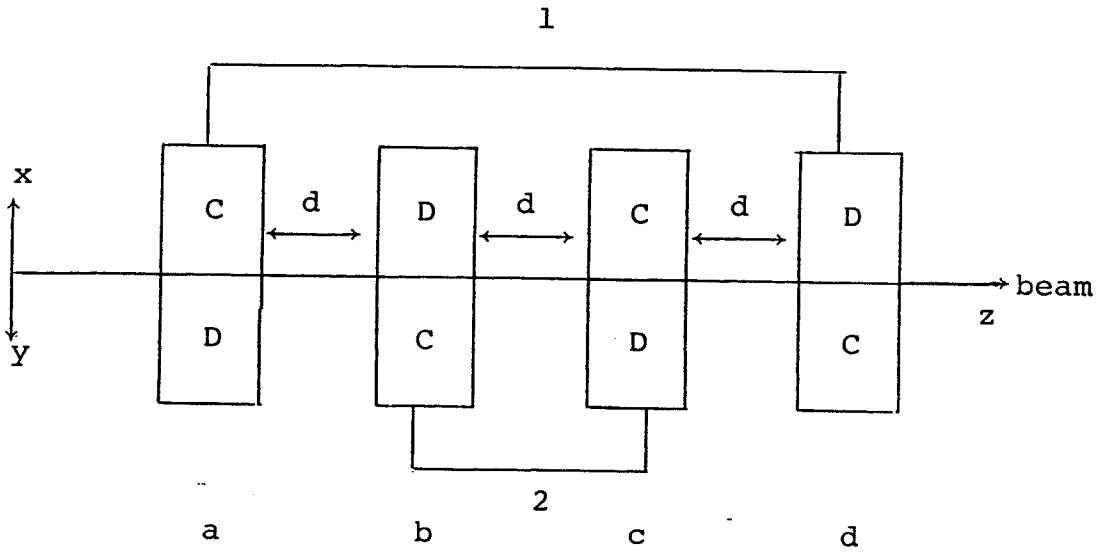

The figure above shows the lens structure in the xz-plane (above the axis) and in the yz-plane (below the axis). The outer two quadrupoles have the same magnetic strength which differs from the value of the magnetic strength of the inner two. We choose subscript 1 to represent the outer two (a and d) and subscript 2 for the inner two (b and c). Since all the separations or drift spaces (the field-free regions between the quadrupoles) have the same dimension d, we denoted the transfer matrix for each one by S. The transfer matrices for the individual elements of the system[25] (in the xz-plane) are listed below:

$$P_{xa} = \begin{vmatrix} \cos \beta_1 & \frac{1}{k_1} \sin \beta_1 \\ -k_1 \sin \beta_1 & \cos \beta_1 \end{vmatrix}$$

$$P_{xb} = \begin{vmatrix} \cosh \beta_2 & \frac{1}{k_2} \sinh \beta_2 \\ k_2 \sinh \beta_2 & \cosh \beta_2 \end{vmatrix}$$

$$P_{xc} = \begin{vmatrix} \cos \beta_2 & \frac{1}{k_2} \sin \beta_2 \\ -k_2 \sin \beta_2 & \cos \beta_2 \end{vmatrix}$$

$$P_{xd} = \begin{vmatrix} \cosh \beta_1 & \frac{1}{k_1} \sinh \beta_1 \\ k_1 \sinh \beta_1 & \cosh \beta_1 \end{vmatrix}$$

$$S = \begin{vmatrix} 1 & d \\ 0 & 1 \end{vmatrix}$$

Where the subscript x indicates that the matrix is for the xz-plane.

Also, $\beta_1 = k_1 L$, $k_1 = \left(\frac{eG_1}{mv}\right)^{\frac{1}{2}}$

$$\beta_2 = k_2 L \quad , \quad k_2 = \left(\frac{eG_2}{mv}\right)^{\frac{1}{2}}$$

d = separation distance between magnets

e = electron charge

m = particle mass

v = particle velocity

G = magnetic field gradient within the aperture $\left(\frac{dB}{da}\right)$

L = effective length of the magnet, defined as

$L = \ell + 1.1\ a$

where ℓ = physical length of the pole piece and a is the radius of the aperture.

The overall transfer matrix of the lens system can be found by matrix multiplication of the above element matrices in the backward order relative to the direction of the beam as:

$$T_x = P_{xd} \times S \times P_{xc} \times S \times P_{xb} \times S \times P_{xa}$$

Multiply out, T_x can be written as

$$T_x = \begin{vmatrix} M_{11} & M_{12} \\ M_{21} & M_{22} \end{vmatrix}$$

which is the resultant matrix of the multiplication of the above seven 2x2 matrices.

Similarly, for the yz-plane, the individual element matrices are:

$$P_{ya} = \begin{vmatrix} \cosh \beta_1 & \frac{1}{k_1} \sinh \beta_1 \\ k_1 \sinh \beta_1 & \cosh \beta_1 \end{vmatrix}$$

$$P_{yb} = \begin{vmatrix} \cosh \beta_2 & \frac{1}{k_2} \sin \beta_2 \\ k_2 \sin \beta_2 & \cos \beta_2 \end{vmatrix}$$

$$P_{yc} = \begin{vmatrix} \cosh \beta_2 & \frac{1}{k_2} \sinh \beta_2 \\ k_2 \sinh \beta_2 & \cosh \beta_2 \end{vmatrix}$$

$$P_{yd} = \begin{vmatrix} \cos \beta_1 & \frac{1}{k_1} \sin \beta_1 \\ k_1 \sin \beta_1 & \cos \beta_1 \end{vmatrix}$$

$$S = \begin{vmatrix} 1 & d \\ 0 & 1 \end{vmatrix}$$

The subscript y indicates that the matrix is for the yz-plane. The final transfer matrix of the lens system in this plane is:

$$T_y = P_{yd} \times S \times P_{yc} \times S \times P_{yb} \times S \times P_{ya}$$

Multiply out, and the resultant matrix T_y may be written as:

$$T_y = \begin{vmatrix} N_{11} & N_{12} \\ N_{21} & N_{22} \end{vmatrix}$$

Now that we have the transfer matrices of the quadruplet lens system, the optical parameters can be easily obtained.

In the xz-plane,

the focal plane on the object side of the lens has a distance from the entrance of the first quadrupole given by:

$$F_{ox} = -\frac{M_{22}}{M_{21}}$$

and on the image side, the focal plane is located at a distance from the exit of the last quadrupole given by:

$$F_{ix} = -\frac{M_{11}}{M_{21}}$$

the principal planes are given by:

$$H_{ox} = \frac{(1 - M_{22})}{M_{21}}$$

and

$$H_{ix} = \frac{(1 - M_{11})}{M_{21}}$$

The focal distances which are the distances between the focus and the corresponding principal plane are defined as:

$$f_{ox} = -\frac{M_{11}}{M_{21}} - \frac{(1 - M_{11})}{M_{21}} = -\frac{1}{M_{21}}$$

and

$$f_{ix} = -\frac{M_{22}}{M_{21}} - \frac{(1 - M_{22})}{M_{21}} = -\frac{1}{M_{21}}$$

therefore $f_{ox} = f_{ix}$

In a similar fashion for the yz-plane, we can arrive at these relations for the optical properties:

$$F_{oy} = -\frac{N_{22}}{N_{21}} \qquad H_{oy} = \frac{(1 - N_{22})}{N_{21}}$$

$$F_{iy} = -\frac{N_{11}}{N_{21}} \qquad H_{iy} = \frac{(1 - N_{11})}{N_{21}}$$

$$f_{oy} = -\frac{1}{N_{21}} \qquad \text{and} \qquad f_{iy} = -\frac{1}{N_{21}}$$

and so $f_{oy} = f_{iy}$

In the two resultant matrices of xz- and yz-planes it can be shown that:

$$M_{21} = N_{21} \qquad \text{and} \qquad M_{12} = N_{12}$$

therefore $f_{ox} = f_{ix} = f_{oy} = f_{iy} = f$

Other optical parameters such as, the magnification, the object distance and the image position can be related to the transfer matrices of the system by multiplying the lens matrix with the two matrices representing those two regions, i.e. the object and the image sides.

Let us denote the object distance by V and the image distance by W. Therefore, the complete transfer from the object to the image point (in the xz-plane) is given by:

$$\begin{vmatrix} x_i \\ x_i' \end{vmatrix} = \begin{vmatrix} 1 & W_x \\ 0 & 1 \end{vmatrix} \times \begin{vmatrix} M_{11} & M_{12} \\ M_{21} & M_{22} \end{vmatrix} \times \begin{vmatrix} 1 & V_x \\ 0 & 1 \end{vmatrix} \times \begin{vmatrix} x_0 \\ x_0' \end{vmatrix}$$

Where the dashed coordinates are representing the divergence angles of the beam

$$x_i = (M_{11} + W_x M_{21})\, x_0 + [V_x (M_{11} + W_x M_{21}) + M_{12} + W_x M_{22}]\, x_0' \quad \ldots\ldots (1)$$

$$x_i' = M_{21}\, x_0 + (V_x M_{21} + M_{22})\, x_0' \quad \ldots\ldots (2)$$

These are the first order particle coordinates at the image plane.

From equation (1) we require x_i to be independent[10,25,26] of x_0' therefore $M_{21} V_x W_x + M_{11} V_x + M_{22} W_x + M_{12} = 0$

$$V_x = - \frac{(W_x M_{22} + M_{12})}{(W_x M_{21} + M_{11})}$$

and

$$W_x = - \frac{(V_x M_{11} + M_{12})}{(V_x M_{21} + M_{22})}$$

The demagnification is given by:

$$g_x = \frac{x_i}{x_o} = M_{11} + W_x M_{21}$$

Substitute for W_x from above and, assume the determinant of the transfer matrix $(M_{11} M_{22} - M_{12} M_{21})$ to be unity since the space on both sides of the lens combination is at the same potential. This gives:

$$g_x = \frac{1}{(V_x M_{21} + M_{22})}$$

Similarly for the yz-plane, we can show that particle coordinates at the image plane are:

$$y_i = (N_{11} + W_y N_{21}) y_o + [V_y(N_{11} + W_y N_{21}) + N_{12} + W_y N_{22}] y'_o \quad \ldots\ldots (3)$$

$$y'_i = N_{21} y_o + (V_y N_{21} + N_{22}) y'_o \quad \ldots\ldots (4)$$

$$V_y = - \frac{(W_y N_{22} + N_{12})}{(W_y N_{21} + N_{11})}$$

$$W_y = - \frac{(V_y N_{11} + N_{12})}{(V_y N_{21} + N_{22})}$$

and

$$g_y = \frac{1}{(V_y N_{21} + N_{22})}$$

For optimum system performance, it is necessary that the geometrical images in both xz- and yz-planes coincide at the exact position of the exit of the lens system regardless of their initial divergence angles and produce a stigmatic image. Therefore, $V_x = V_y = V$ and of course we should have $W_x = W_y = W$. In our particular structure, the "Russian quadruplet", the two resultant transfer matrices give $M_{11} = N_{11}$ and $M_{22} = N_{22}$, so that the demagnification in both planes is

the same, that is $g_x = g_y = g$.

3.2 Matrix expansion to third order coordinates

The above analysis of the matrix method was made in this fashion to show clearly and simply how the probe-forming system acts on a beam of particles independently in the xz- and yz-planes. However, when writing a computer program to calculate the exit coordinates of the beam, it is common to combine the matrices for both planes into one and then to derive the overall transfer matrix of the system.

The first order overall matrix will be written as:

$$\begin{vmatrix} x_i \\ y_i \\ x'_i \\ y'_i \\ \delta \end{vmatrix} = \begin{vmatrix} C_{11} & 0 & C_{13} & 0 & 0 \\ 0 & C_{22} & 0 & C_{24} & 0 \\ C_{31} & 0 & C_{33} & 0 & 0 \\ 0 & C_{42} & 0 & C_{44} & 0 \\ 0 & 0 & 0 & 0 & 1 \end{vmatrix} \times \begin{vmatrix} x_o \\ y_o \\ x'_o \\ y'_o \\ \delta \end{vmatrix}$$

Where the above matrix elements are those coefficients given in equations (1) to (4) . δ is the fractional momentum-spread which is not affected by the focusing system.

Although the above method is acceptable for initial calculations of the beam coordinates when passing through a lens system, it has very

limited application in practice. This limitation comes from not considering any of the higher order aberration effects which are always in existence in an optical system. While the particle coordinates can be represented by a polynomial series, terms of order higher than the third have negligible effect on the final beam size. Thus, transfer matrices containing terms up to the third order are sufficiently accurate for beam optic calculations.

As we mentioned before, the third order transfer matrix of the system may be obtained easily by substituting the third order matrix for each system element for the first order matrix. The third order matrix contains 55x55 matrix elements, instead of the 5x5 first order matrices we described earlier. The second and the third order matrix elements which begin at the sixth row can be derived by simple algebraic operations from the first order elements[10]. At the end of the matrix multiplication of all the lens elements, we will arrive at the final transfer matrix of the system which can be written as:

$$
\begin{vmatrix} x_i \\ y_i \\ x_i' \\ y_i' \\ \delta \\ x_i^2 \\ x_i y_i \\ \vdots \\ \vdots \\ \vdots \end{vmatrix}
=
\begin{vmatrix} F_{11} & F_{12} & \cdots & F_{1\,55} \\ F_{21} & F_{22} & \cdots & F_{2\,55} \\ \vdots & \vdots & & \vdots \\ \vdots & \vdots & & \vdots \\ \vdots & \vdots & & \vdots \\ \vdots & \vdots & & \vdots \\ \vdots & \vdots & & \vdots \\ \vdots & \vdots & & \vdots \\ \vdots & \vdots & & \vdots \\ F_{55\,1} & F_{55\,2} & \cdots & F_{55\,55} \end{vmatrix}
\times
\begin{vmatrix} x_o \\ y_o \\ x_o' \\ y_o' \\ \delta \\ x_o^2 \\ x_o y_o \\ \vdots \\ \vdots \\ \vdots \end{vmatrix}
$$

The elements of the above matrix now contain a large number of terms, and considering the 55x55 number of elements in the matrix, the computation is complicated and time consuming. However, an important fact worth mentioning here is that more than one third of the third order matrix elements are zeroes[10]. This fact can be exploited when designing computer programs to reduce the multiplication time and make the program more efficient.

CHAPTER 4

DESIGN CONSIDERATIONS AND OPTIMIZATION OF BEAM OPTICS

CHAPTER 4

DESIGN CONSIDERATIONS AND OPTIMIZATION OF BEAM OPTICS

In 1983, a feasibility study aimed at designing a proton microprobe at the University of Manitoba Cyclotron laboratory was completed[21]. It was based on an estimate of the available space area and the system was to focus proton beams in the energy range of 20-50 MeV within an object-to-image distance of 4.39 m. This study, which considered only the first order parameters of the beam, showed very encouraging results and suggested that an image 10x10 μm^2 in size[18,21,22] was obtainable. However, practice has proven that higher order parameters introduce large effects and add an important contribution in determining the actual beam spot size at the Gaussian image plane.

In this present study, the beam optics of the design have been analyzed thoroughly with the aid of two computer programs (IONBEAM and IMAGE8). An analysis up to third order was made using these programs. They were broadly investigated in order to achieve the optimum set of system parameters such as: 1) Separation distance, 2) object distance, 3) image distance, 4) shape function of the fringing field, and 5) beam emittance. The program IONBEAM has the capacity to perform an optimization process on the lens parameters in order to yield the best image. Therefore it was employed throughout the main analysis. The

program IMAGE8, which has been developed at the Physics Department of the University of Manitoba, is a modified version of Matsuda's TRIO program. The function of the program IMAGE8 is to utilize the data of the lens parameters, which are derived from TRIO, to trace any specified number of beam particles from the object plane to the image plane using a Monte Carlo simulation technique. This program was used to display the proton distribution at the Gaussian image plane. Furthermore, it was useful for verification of the data obtained from program IONBEAM.

4.1 Beam optics analysis and lens performance

The analysis was based on an object size of 70x70 μm^2. We carried out several investigations in order to observe the effects on spot size and the required magnetic fields by varying one or more of the above mentioned system parameters. The goal was to accomplish a comprehensive picture of the system's behaviour under various conditions in order to decide upon the most practical features for our microprobe system.

Since quadrupoles cannot be built ideally, there are other field harmonic contaminations present in the field within the magnet bore. A flipping coil Gaussmeter device was assembled to measure the differential magnetic field ($\Delta B/B$) along the median plane (which is any plane containing the lens axis) of one of the four identical quadrupoles. The radius of the magnet aperture is 27 mm. Figure 4.1 shows that the differential field is constant only within a circle of 15 mm in radius.

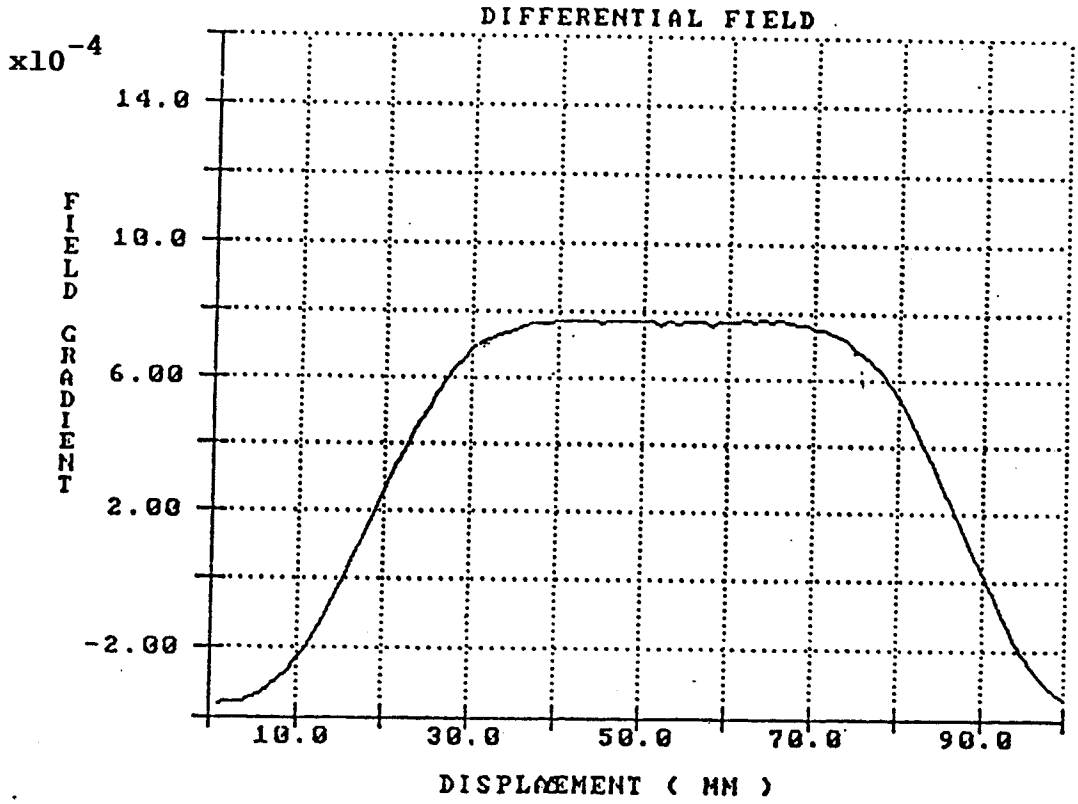

Figure 4.1 The differential field variation inside the quadrupole magnet along the median plane.

This is in agreement with the theory and pointed out by Grime and Watt[10] which outlines that the higher the order of the harmonic, the more concentrated it is at larger radii. Our distance of constant field gradient represents 0.56r (r is the radius) compared to the 0.73r and 0.9r estimated by Grime and Watt[10] and Banford[27] respectively for the same pole shape. Therefore, during our analysis we had to ensure that the radius of the beam envelope did not exceed 15 mm in order to minimize the effect of the higher field harmonics in the actual system.

Even though the calculations were carried out to include up to the third order parameters, the third order mode of the program IONBEAM was not activated initially to perform these calculations. This is due to the fact that a large amount of computer time is consumed for each execution and, taking the long searching procedure into account, this became an inefficient process. The first order mode was utilized until an optimum was found. This optimum was then employed in the third order mode of calculation.

During optimization, a number of parameters are defined as variables. They are changed in order to achieve certain specified conditions. The range of variation of these variables is defined by the user. The size of the specified range is found to have no effect on the outcome as long as the optimum values fall within these limits. Therefore, it was a useful practice to define a broad range for the variation throughout our study to ensure the inclusion of the optimum. The formation of a stigmatic image (i.e. one in which the images of an

object in xz- and yz-planes coincide in one xy-plane) is very sensitive to the magnetic field values, out to the fifth decimal place. Therefore, power supplies with long-term stability ($\Delta I/I \leq 10^{-5}$) are essential.

Theoretically, the perfect stigmatic image is located at a plane where the coefficients (x/θ) and (y/ϕ) of the transfer matrix of the system have zero values[11,25,34] as shown in chapter (3). This condition is due to the fact that at this plane the point-to-point image[26] is independent of the divergence angles θ and ϕ. However, this condition could not be reached during the optimization procedure because of the limitations of the optimization technique. Small values for these coefficients, on the order of 10^{-4} or less, were considered to be close enough to zero to indicate the achievement of the stigmatic image. The effect of these approximations has been examined and found to be $\pm$ 0.01 μm in each of the xz- and yz-planes of the first order image. This uncertainty is negligible compared to the image dimensions as will be shown next.

4.1.1 Analysis of the optical parameters of the microprobe lens

In the previous study[21], analysis was based on the latest available data on the beam emittance of the Manitoba cyclotron before the recent improvement of beam quality took place. Since new data on the beam emittance were not available during our analysis, we utilized the same data (the emittance of 35.34 mm.mrad and 22.81 mm.mrad in xz-

and yz-planes respectively). Hence, it was very important at the beginning of our study to realize the effects of the initial beam divergence on the focused microbeam. The improvement to our cyclotron beam resulted in better emittance and higher current density. The first investigation was to observe the influence of partial divergences with respect to those adopted in our analysis. While no effect was noticed on the first order spot size caused by varying the beam divergences, there are significant effects on the aberrations, as will be shown later. In general, the smaller the divergences, the less the aberration contribution to the beam spot size. The second factor which had to be investigated at the very beginning was the separation distance between the quadrupole magnets. The minimum available spacing due to construction limitations made it essential to understand the effect of such factors on the lens performance. Unequal separations between all the quadrupoles have been found to be very destructive and worsen the beam parameters. Therefore we select equal separations only and this is shown in figure 4.2. Clearly, the smaller the separation distance, the smaller the image size achieved, though higher magnetic field settings are required. We can see from this figure that at a separation of 8 cm, which was conservatively chosen, the image dimensions were increased by 13% from that at zero separation. However, the required focusing field was decreased by 33% for the higher field magnets (second and third quadrupoles) and by 23% for the lower field magnets (first and fourth quadrupoles).

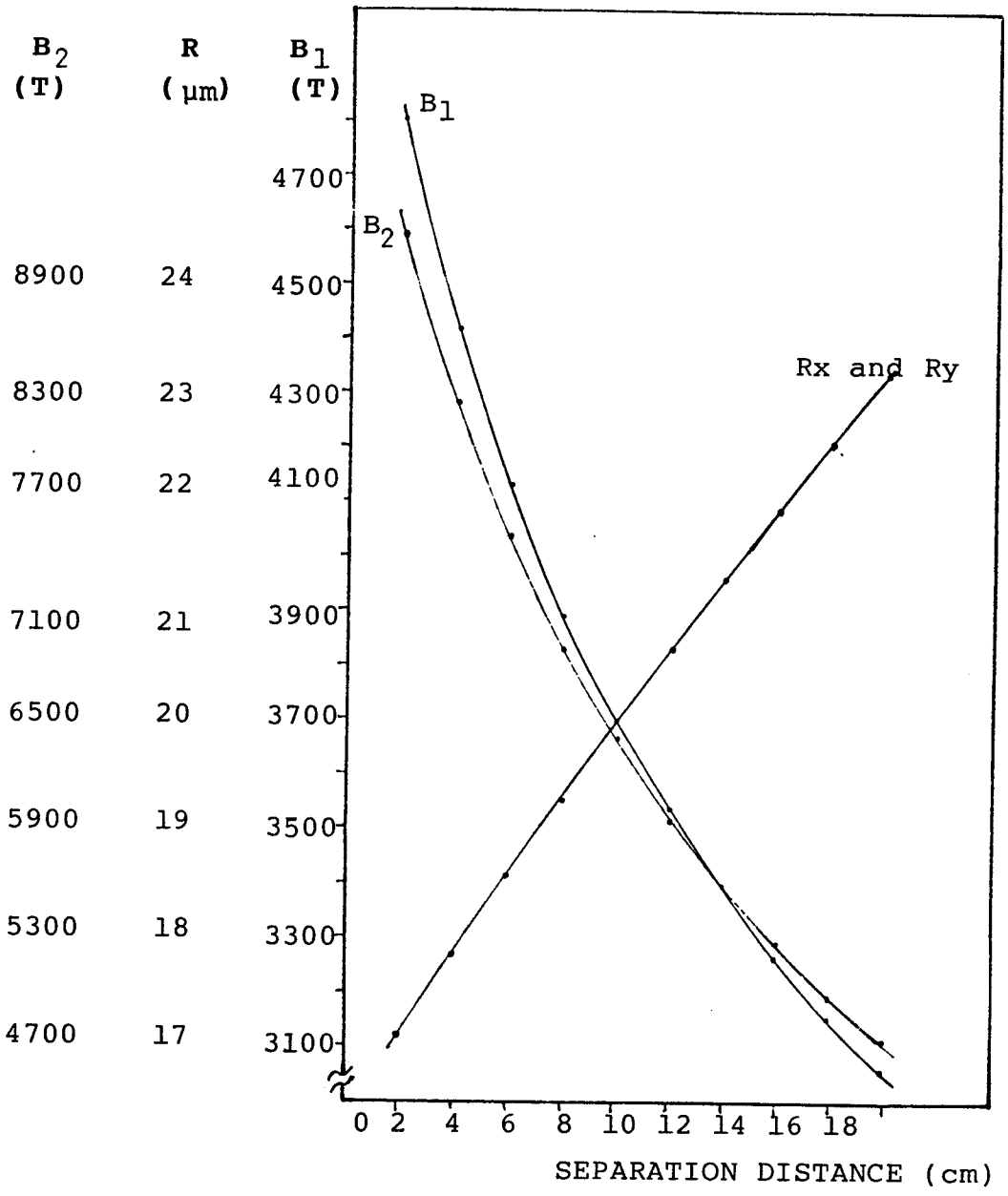

Figure 4.2 The variation of the image dimensions and the required excitations with the separation distance between adjacent quadrupoles. R_x and R_y are half the dimension in x and y coordinates. Image distance, 0.03 m, object distance, 0.758m and beam energy, 50 MeV for the quadruplet.

B_1: the magnetic field setting of the outer two quadrupoles

B_2: the magnetic field setting of the inner two quadrupoles

Based on an 8 cm separation distance, we proceeded to investigate the influence of other parameters on the microprobe performance. At this stage the effects of the image distance were not available. Therefore, to examine the influence of the object distance (from the 15° object slit to the entrance of the first quadrupole) on the image size, an image distance (from the exit of the last quadrupole to the Gaussian image plane) of 3 cm was arbitrarly chosen. Figure 4.3 shows the relation between image size and object distance, which are normalized in terms of the effective length of the quadrupoles (L), while holding all other parameters fixed. There is an important observation which is worth mentioning here. When the object distance exceeds twenty times L and the image size becomes smaller and smaller, the stigmatic image becomes more difficult to achieve. This is due to its high sensitivity to the magnetic field values (to the eighth decimal place when the object distance becomes 30 times L).

A mutual analysis was carried out to visualize the influence of object distance variation, on the image size at various image distances. This was done by using the same range of object distances each time at a given image distance while all other beam parameters were fixed. Figure 4.4 shows the relationship between image size and the image distance for a distance up to the effective length of quadrupole (L), at 1.458 m object distance. The same results are listed in table 4.1 with the values of the excitations required each time. As can be seen, increasing the image distance has an adverse effect on demagnification, though the required magnetic fields are reduced.

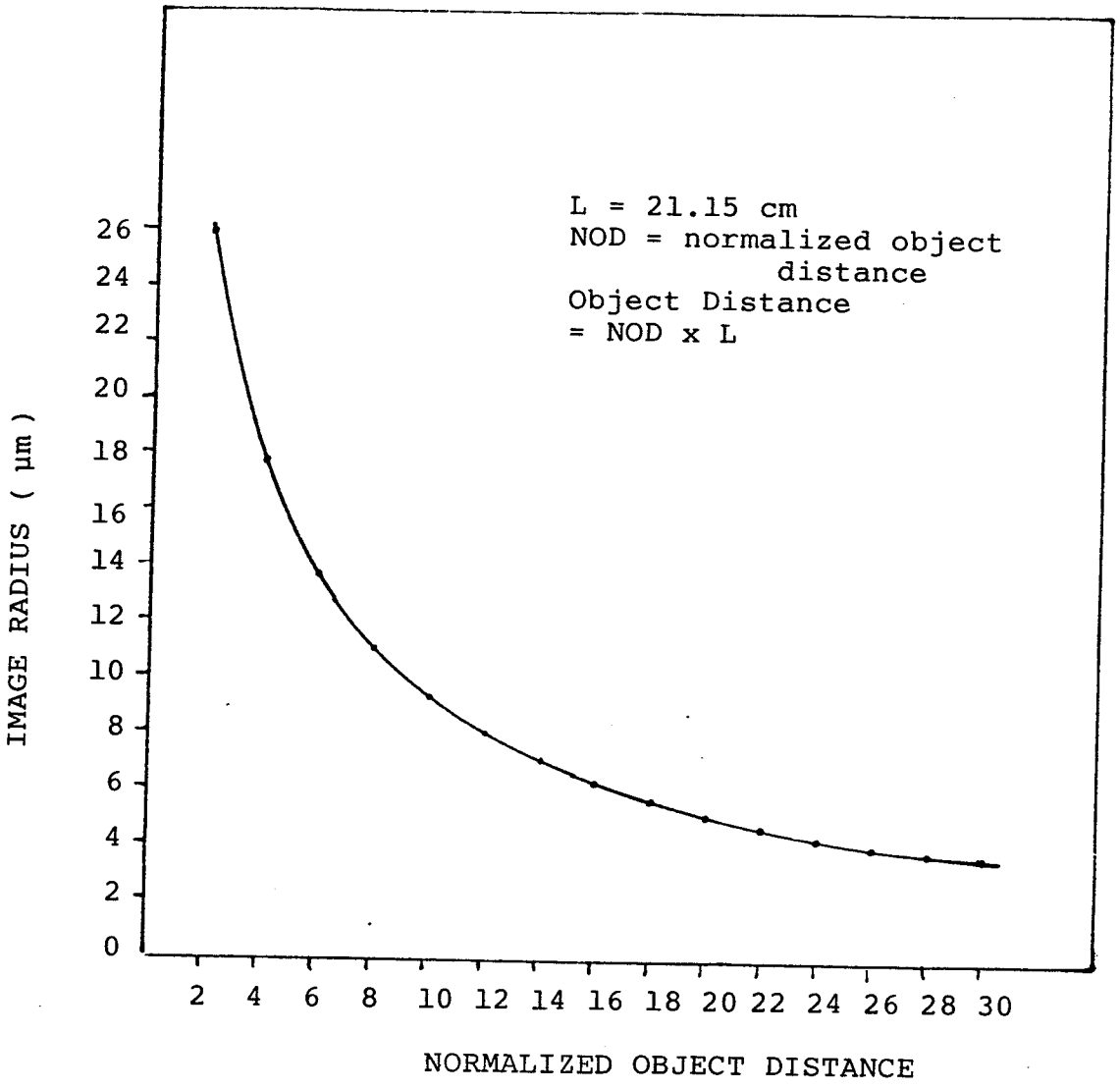

Figure 4.3 The relationship between the normalized object distance (with respect to the effective length) and the image radius at image distance, 3 cm and separation distance, 8 cm for the quadruplet.

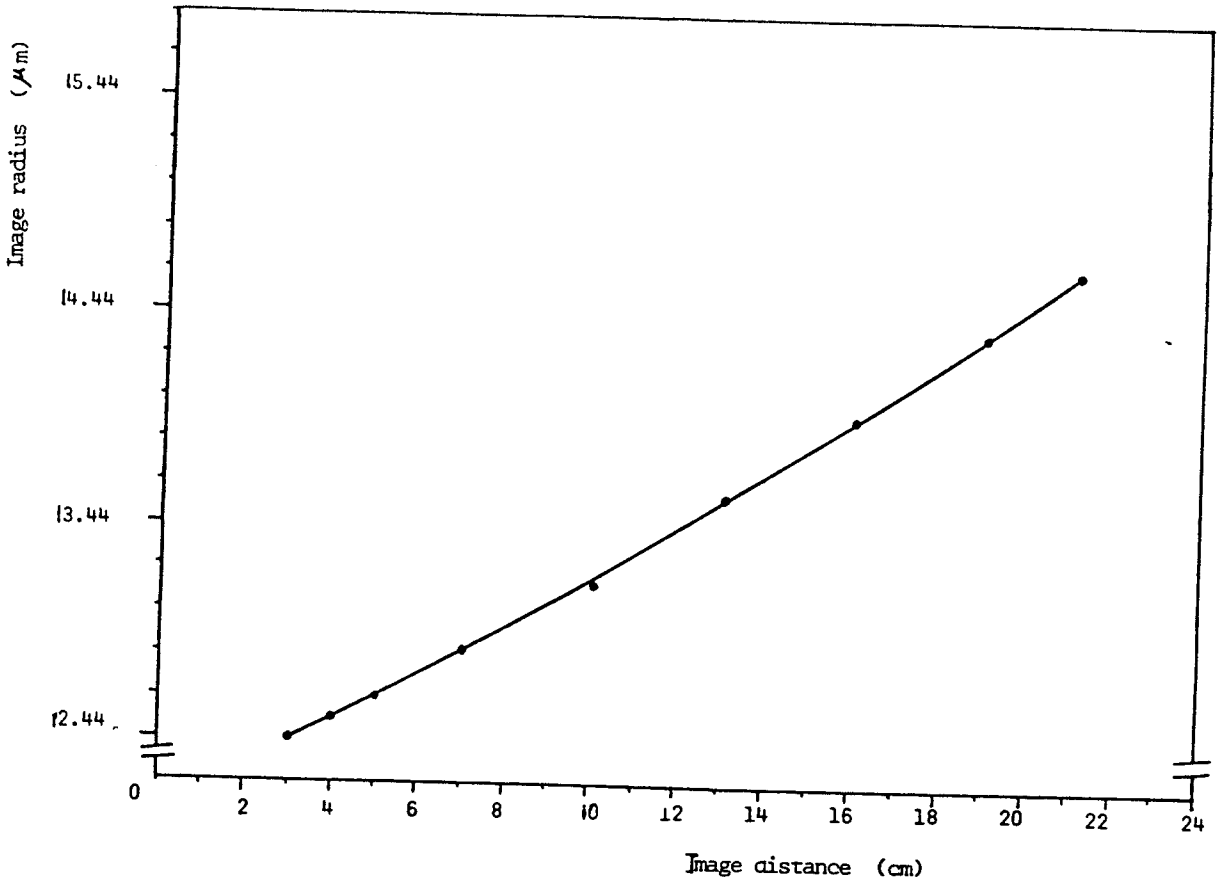

Figure 4.4 The variation of the image radius with the image distance for an object distance of 1.458 m and separation distance of 8 cm for the quadruplet.

IMAGE DISTANCE (m)	Rx (μm)	Ry (μm)	$\mp B_1$ (T)	$\mp B_2$ (T)
0.03	12.44	12.44	0.3229	0.6326
0.04	12.54	12.54	0.3187	0.6285
0.05	12.64	12.64	0.3146	0.6245
0.07	12.86	12.86	0.3069	0.6168
0.10	13.21	13.21	0.2962	0.6056
0.13	13.58	13.58	0.2864	0.5950
0.16	13.96	13.96	0.2776	0.5850
0.19	14.36	14.36	0.2695	0.5756
0.2115	14.66	14.66	0.2641	0.5691

Table 4.1 Half-dimensions of the image in x and y coordinates and the magnetic fields (+ve: focus in x, defocus in y and -ve: defocus in x, focus in y) as a function of image distance at object distance, 1.458m, lens separation distance, 8 cm and beam energy, 50 MeV (magnetic quadruplet)
B_1: the magnetic field setting of the outer two quadrupoles
B_2: the magnetic field setting of the inner two quadrupoles

Practically, the image has to be at some distance from the exit to allow some space to place the target and detection assemblies. Fortunately, an image distance of 10 cm has increased the spot size by only 6.2% compared to a 3 cm image distance. An image distance of 21.15 cm would increase the spot size by 17.8%. A 10 cm image distance was chosen for our microprobe arrangement. For this image distance, the variation of the image size with object distance and magnetic field is shown in figure 4.5 and table 4.2. The range of variations of object distance, from 0.658 m up to 2.115 m (10 times the effective length of a single quadrupole). Within this range the improvement of image size is 120% (largest image at the shortest distance and decreasing by 120% at the largest image distance). At the same time, the magnetic fields are reduced by about 33% for the outer two and 14.6% for the centre two quadrupoles.

It was decided that in order to maintain high stability and keep vibration effects as small as possible, the whole microprobe unit had to be mounted on one table. Initially an object distance of 1.358 m was thought to be acceptable. However, this calculation shows that we could decrease the spot size by 24% and the magnetic field by 7% (outer magnets) and 3.5% (inner magnets) by choosing an object distance of 1.808 m. This object distance can readily be tolerated while maintaining the required high stability.

Once we have the distances and other beam parameters fixed, the variation in beam energy will have no effect on the demagnifying power

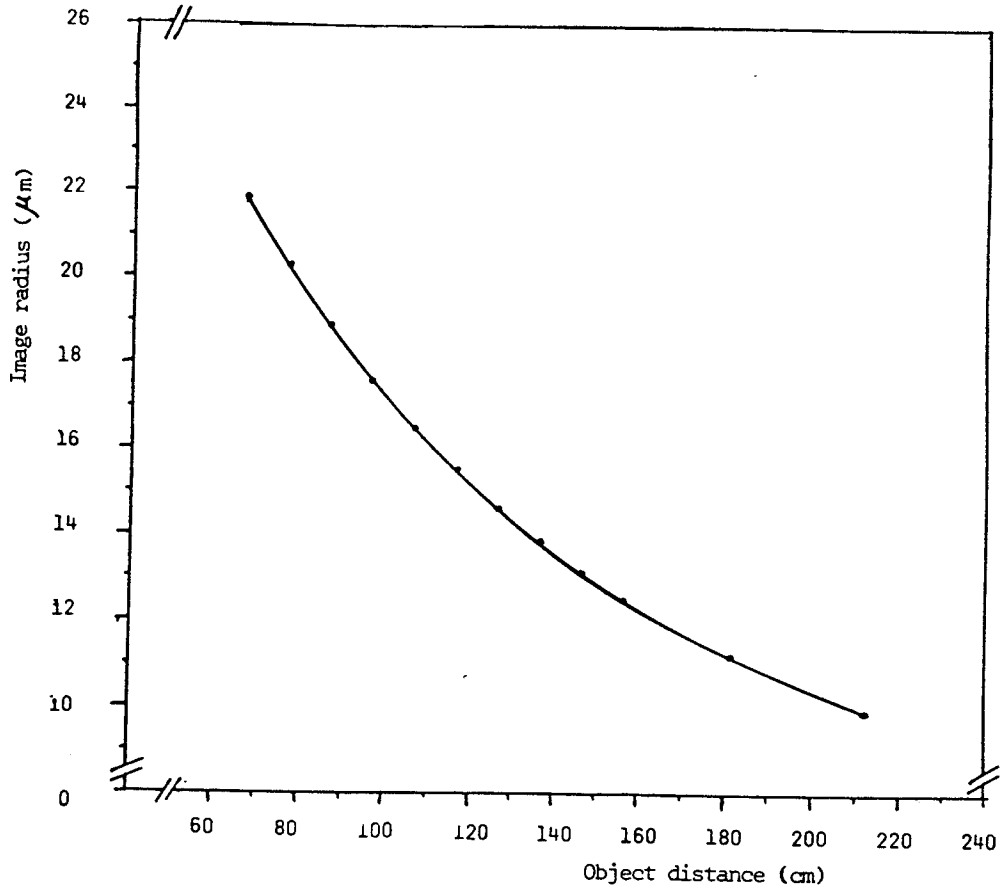

Figure 4.5 The variation of the image radius with the object distance at image distance, 10 cm and separation distance, 8 cm for the quadruplet.

OBJECT DISTANCE (m)	Rx (μm)	Ry (μm)	$\mp B_1$ (T)	$\mp B_2$ (T)
0.658	21.87	21.87	0.3711	0.6748
0.758	20.25	20.25	0.3549	0.6614
0.858	18.84	18.84	0.3417	0.6500
0.958	17.60	17.60	0.3309	0.6401
1.058	16.51	16.51	0.3217	0.6314
1.158	15.55	15.55	0.3139	0.6238
1.258	14.68	14.68	0.3072	0.6171
1.358	13.91	13.91	0.3013	0.6110
1.458	13.21	13.21	0.2962	0.6056
1.558	12.59	12.59	0.2956	0.6097
1.808	11.24	11.24	0.2860	0.5991
2.115	9.93	9.93	0.2771	0.5888

Table 4.2 Half-dimensions of the image in x and y coordinates and the magnetic fields (+ve: focus in x, defocus in y and -ve: defocus in x, focus in y) as a function of object distance at image distance, 10cm, lens separation distance, 8 cm and beam energy, 50 MeV (magnetic quadruplet)
B_1: the magnetic field setting of the outer two quadrupoles
B_2: the magnetic field setting of the inner two quadrupoles

of the system. However, the necessary magnetic fields will increase for higher beam energies. This is shown in table 4.3. Notice that the demagnifying power and the required field settings are independent of the initial beam size and divergence angles if everything else is the same.

4.1.2 Optical characteristics of the pre-microprobe lens (magnetic doublet)

In order to achieve the spot size required with an optimum current intensity from the microprobe quadruplet, the proton beam has to be prepared according to certain conditions after leaving the cyclotron. This can be accomplished through an intermediate magnetic doublet lens which was chosen for this purpose. A separate, but similar analysis to that for the microprobe which was described in section 4.1.1, was carried out for the doublet. The results are summarized in tables 4.4 and 4.5. When the separation distance increases the required magnetic fields decrease. However, the effect on the spot size is not the same for both xz- and yz-planes (table 4.4). As the separation distance increases the spot dimension in the xz-plane becomes larger, and in the yz-plane, it becomes smaller.

When the image distance increases while all the other parameters are fixed, again the effect is a lower magnetic field setting. However, the influence on the beam spot size is to produce a larger dimension in both planes (table 4.5). Although the initial divergence of the beam at

BEAM ENERGY (Mev)	Rx (μm)	Ry (μm)	$\mp B_1$ (T)	$\mp B_2$ (T)
20	11.24	11.24	0.1795	0.3759
25	11.24	11.24	0.2010	0.4208
30	11.24	11.24	0.2204	0.4616
35	11.24	11.24	0.2384	0.4993
40	11.24	11.24	0.2552	0.5344
45	11.24	11.24	0.2710	0.5676
50	11.24	11.24	0.2860	0.5991

Table 4.3 Half-dimensions of the image in x and y coordinates and the magnetic fields (+ve: focus in x, defocus in y and -ve: defocus in x, focus in y) as a function of beam energy at object distance, 1.808m, image distance, 10cm and lens separation distance, 8 cm (magnetic quadruplet)
B_1: the magnetic field setting of the outer two quadrupoles
B_2: the magnetic field setting of the inner two quadrupoles

SEPARATION DISTANCE (m)	Rx (μm)	Ry (μm)	B_1 (T)	$-B_2$ (T)
0.10	2.018	1.135	0.3123	0.3676
0.12	2.045	1.128	0.3017	0.3575
0.14	2.073	1.120	0.2921	0.3483
0.16	2.101	1.112	0.2833	0.3400
0.18	2.129	1.104	0.2752	0.3324
0.20	2.158	1.096	0.2677	0.3254
0.22	2.187	1.088	0.2608	0.3190
0.24	2.215	1.081	0.2544	0.3130
0.26	2.244	1.073	0.2484	0.3075
0.28	2.273	1.066	0.2428	0.3023
0.30	2.302	1.058	0.2376	0.2975

Table 4.4 Half-dimensions of the image in x and y coordinates and the magnetic fields of the doublet (+ve: focus in x, defocus in y and -ve: defocus in x, focus in y) as a function of magnet separation distance at object distance, 3.741m, image distance, 1.247m and beam energy, 50 MeV.
B_1: the magnetic field setting of the first quadrupole in the beam direction
B_2: the magnetic field setting of the second quadrupole in the beam direction

IMAGE DISTANCE (m)	Rx (μm)	Ry (μm)	B_1 (T)	$-B_2$ (T)
1.247	2.738	1.389	0.3116	0.3601
1.347	2.860	1.499	0.3062	0.3479
1.447	2.982	1.611	0.3013	0.3371
1.547	3.104	1.722	0.2968	0.3276
1.647	3.226	1.835	0.2927	0.3191
1.747	3.348	1.948	0.2889	0.3114
1.847	3.470	2.061	0.2853	0.3045
1.947	3.592	2.175	0.2820	0.2983
2.047	3.714	2.289	0.2790	0.2926
2.147	3.836	2.405	0.2761	0.2874

Table 4.5 Half-dimensions of the image in x and y coordinates and the magnetic fields of the doublet (+ve: focus in x, defocus in y and -ve: defocus in x, focus in y) as a function of image distance at object distance, 2.841m, magnet separation distance, 14 cm and beam energy, 50 MeV.

B_1: the magnetic field setting of the first quadrupole in the beam direction

B_2: the magnetic field setting of the second quadrupole in the beam direction

the object plane has no effect on the first order image size, as we have found in the last section, it has a dramatic influence on the second and third order aberrations as will be shown in the next section. Therefore, a compromise had to be made in order to achieve an image with acceptable divergence angles from the doublet. The image has to be large enough to have reasonable divergence angles but not so large that we lose most of the beam through collimation by the microprobe object slit. The chosen structure is shown in the seventh row of table 4.6.

4.2 Higher order aberrations and fringing field effects

There are eight significant high order aberration coefficients which affect the spot size of a beam focused by a quadrupole lens system[28]. There are four chromatic aberration coefficients of the second order which are mainly associated with the energy or momentum spread of the incoming beam. The other four are spherical aberration coefficients which are influenced by the initial divergences of the beam at the object plane[5]. The effect on these coefficients of changing the image distance is shown in table 4.7. All the coefficients associated with the xz-plane are increased when we increase the image distance. However, the coefficients which are associated with the yz-plane show the opposite relation with the image distance except $\langle y/\theta^2\phi \rangle$. In table 4.8, the values of the aberration coefficients at various object distances are listed. At larger object distances all the aberration coefficients increase except $\langle y/y\delta \rangle$ which decreases. As the data shows, the change in these high order coefficients with the image distance is

OBJECT DISTANCE (m)	IMAGE DISTANCE (m)	SEPARATION DISTANCE (m)	Rx (mm)	Ry (mm)	B_1 (T)	$-B_2$ (T)
3.741	1.247	0.08	1.991	1.143	0.3240	0.3788
2.841	1.247	0.00	2.499	1.463	0.4110	0.4570
2.841	2.147	0.08	2.630	1.423	0.3447	0.3921
2.341	1.247	0.08	3.197	1.647	0.3626	0.4028
2.341	1.247	0.14	3.326	1.603	0.3285	0.3696
2.341	1.647	0.20	4.060	2.050	0.2862	0.3057
*2.241	2.147	0.20	5.040	2.800	0.2759	0.2780
1.441	2.347	0.08	7.902	4.314	0.3791	0.3509

Table 4.6 Half-dimensions of the image in x and y coordinates and the magnetic fields of the doublet (+ve: focus in x, defocus in y and -ve: defocus in x, focus in y) at various selected conditions of object, image and separation distances at beam energy, 50 MeV.
B_1: the magnetic field setting of the first quadrupole in the beam direction
B_2: the magnetic field setting of the second quadrupole in the beam direction

* The adopted combination for the final configuration.

IMAGE DISTANCE (m)	CHROMATIC ABERRATION COEFFICIENTS				SPHERICAL ABERRATION COEFFICIENTS				Rx(μm)	Ry(μm)	$\mp B_1$(T)	$\mp B_2$(T)
	$\langle x/\theta\delta \rangle$	$\langle x/x\delta \rangle$	$\langle y/\Phi\delta \rangle$	$\langle y/y\delta \rangle$	$\langle x/\theta^3 \rangle$	$\langle x/\theta\Phi^2 \rangle$	$\langle y/\Phi^3 \rangle$	$\langle y/\theta^2\Phi \rangle$				
0.02	1.231	0.4626	3.347	2.044	-151.7	-353.8	-1563.0	-354.1	13.03	13.03	0.3377	0.6519
0.05	1.324	0.5031	3.240	1.968	-161.5	-370.3	-1495.0	-370.7	13.34	13.34	0.3246	0.6396
0.08	1.414	0.5443	3.154	1.906	-172.4	-386.3	-1437.0	-386.8	13.68	13.68	0.3128	0.6278
0.10	1.472	0.5718	3.106	1.871	-180.0	-396.6	-1402.0	-397.3	13.92	13.92	0.3055	0.6203
0.12	1.528	0.5988	3.065	1.840	-187.9	-406.8	-1371.0	-407.4	14.18	14.18	0.2987	0.6130
0.15	1.609	0.6387	3.014	1.801	-200.0	-421.7	-1330.0	-422.3	14.57	14.57	0.2892	0.6027
0.18	1.687	0.6776	2.974	1.770	-212.2	-436.0	-1294.0	-436.7	14.98	14.98	0.2806	0.5929
0.2115	1.764	0.7169	2.941	1.744	-224.9	-450.7	-1260.0	-451.4	15.43	15.43	0.2723	0.5831

Table 4.7 The main aberration coefficients, half-dimensions of the image in x and y coordinates and the required magnetic fields for the quadruplet (+ve: focus in x, defocus in y and -ve: defocus in x, focus in y) as a function of the image distance at object distance, 1.358m, separation distance, 8cm, energy, 50 MeV and standard fringing field function.
B_1: the magnetic field setting of the outer two quadrupoles
B_2: the magnetic field setting of the inner two quadrupoles

IMAGE DISTANCE (m)	CHROMATIC ABERRATION COEFFICIENTS				SPHERICAL ABERRATION COEFFICIENTS				Rx(μm)	Ry(μm)	$\mp B_1$ (T)	$\mp B_2$ (T)
	$\langle x/\theta\delta \rangle$	$\langle x/x\delta \rangle$	$\langle y/\Phi\delta \rangle$	$\langle y/y\delta \rangle$	$\langle x/\theta^3 \rangle$	$\langle x/\theta\Phi^2 \rangle$	$\langle y/\Phi^3 \rangle$	$\langle y/\theta^2\Phi \rangle$				
0.958	1.231	0.4990	2.571	2.051	-83.38	-196.0	-728.5	-196.3	17.62	17.62	0.3355	0.6499
1.058	1.290	0.5185	2.707	1.997	-102.8	-237.5	-871.0	-237.9	16.53	16.53	0.3262	0.6411
1.158	1.350	0.5406	2.841	1.950	-125.2	-284.6	-1030.0	-285.0	15.56	15.56	0.3183	0.6333
1.258	1.411	0.5579	2.974	1.908	-150.9	-337.5	-1207.0	-338.0	14.70	14.70	0.3115	0.6264
1.358	1.472	0.5718	3.106	1.871	-180.0	-396.6	-1402.0	-397.3	13.92	13.92	0.3055	0.6203
1.558	1.597	0.5917	3.367	1.808	-249.5	-535.0	-1853.0	-535.7	12.59	12.59	0.2956	0.6097
1.808	1.748	0.6079	3.690	1.745	-359.3	-748.8	-2537.0	-749.7	11.24	11.24	0.2860	0.5991
2.115	1.939	0.6200	4.083	1.684	-533.8	-1081.0	-3580.0	-1802.0	9.93	9.93	0.2771	0.5888

Table 4.8 The main aberration coefficient, half-dimensions of the image in x and y coordinates and the required magnetic fields for the quadruplet (+ve: focus in x, defocus in y and -ve: defocus in x, focus in y) as a function of the object distance at image distance, 10 cm, separation distance, 8 cm, energy, 50 MeV and standard fringing field function.
B_1: the magnetic field setting of the outer two quadrupoles
B_2: the magnetic field setting of the inner two quadrupoles

small and therefore our choice of a 10 cm image distance will have a negligible effect on increasing the contribution of these aberrations to the spot size. Similarly the object distance change has a very small effect on the chromatic aberration coefficients, even though the spherical aberration coefficients are almost doubled as the object distance increased from 1.358 m to 1.808 m. This justifies arranging the doublet lens so as to reduce the divergence angles, as will be seen later.

Data on the chromatic and spherical aberration coefficients were initially calculated without including a fringing field, but were later compared to the same data when considering two types of fringing field functions. This data is shown in table 4.9. The chromatic aberration coefficients show little change between the three cases. However, the spherical aberration coefficients are much larger when fringing fields are included, though there are no noticeable differences in their values at various levels of fringing fields. On the other hand, the calculations indicate that the high order aberration coefficients are not a function of the beam energy. There are other types of second order parasitic aberration effects due to rotational misalignments which are dependent upon the divergence angles of the beam. However, they can be reduced by proper adjustment of only one quadrupole element[10].

The effect of the fringing field of a quadrupole lens on the lens performance and characteristics is due to the introduction of both an axial component of the magnetic field and radial components of higher

CONDITION	CHROMATIC ABERRATION COEFFICIENTS				SPHERICAL ABERRATION COEFFICIENTS			
	$\langle x/\theta\delta \rangle$	$\langle x/x\delta \rangle$	$\langle y/\phi\delta \rangle$	$\langle y/y\delta \rangle$	$\langle x/\theta^3 \rangle$	$\langle x/\theta\phi^2 \rangle$	$\langle y/\phi^3 \rangle$	$\langle y/\theta^2\phi \rangle$
no fringing field	1.757	0.6126	3.679	1.738	-233.5	-23.28	-1653.0	-23.27
fr. field type 1	1.750	0.6087	3.687	1.742	-356.5	-744.1	-2510.0	-744.8
fr. field type 2	1.748	0.6079	3.690	1.745	-359.3	-748.8	-2537.0	-749.7

The fringing field integrals are:

type 1: $I_1 = 0.16667$, $I_2 = 0$, $I_3 = 0.06667$, $I_4 = -0.33333$

type 2: $I_1 = 0.2090$, $I_2 = -0.07678$, $I_3 = 0.05518$, $I_4 = -0.3306$ (standard fringing field)

Table 4.9 The values of the main aberration coefficients in the quadruplet for various conditions. Object distance, 1.808m, image distance, 10cm, separation distance, 8cm.

order multipole fields at the end-field regions which extend over a distance approximately equal to the quadrupole bore diameter[10]. Table 4.10 shows the relationship between the object distance, the image size and the magnetic field settings for the three cases, first without fringing field and then with two different fringing fields. It is clear that the field settings are slightly altered by the presence of fringing fields of any kind.

In order to demonstrate the effects of the divergence angles and the energy spread of the proton beam on the final spot size we utilized a Monte Carlo simulation to trace individual particles through the lens system to the Gaussian image plane. The real distribution of intensity in the image plane will depend upon the actual distribution of the incident beam from the object slit. The particle distribution at the object plane, however, was assumed to be homogeneous which is acceptable in our case since the object is the very small collimated area in a relatively large waist of the beam formed by a doublet lens.

The final beam profile at the image plane, which is shown in figure 4.6, was achieved by adopting the data of the divergence angles and energy spread obtained in the previous study. Although more than 80% of the particles fall within the area predicted by the first order image calculations, the contribution from higher order aberrations is seen to be large. In figure 4.7, we have reduced the energy spread to half the value of figure 4.6. The image size was improved mainly in the

CONDITION	OBJECT DISTANCE (m)	Rx (μm)	Ry (μm)	$\bar{+}B_1$(T)	$\bar{+}B_2$(T)
No Fringing Field	1.058	16.51	16.51	0.3217	0.6314
	1.158	15.55	15.55	0.3139	0.6238
	1.258	14.68	14.68	0.3072	0.6171
	1.358	13.91	13.91	0.3013	0.6110
Fringing Field type I	1.058	16.53	16.53	0.3253	0.6390
	1.158	15.56	15.56	0.3174	0.6313
	1.258	14.70	14.70	0.3106	0.6244
	1.358	13.92	13.92	0.3046	0.6183
Fringing Field type 2	1.058	16.53	16.53	0.3262	0.6411
	1.158	15.56	15.56	0.3183	0.6333
	1.258	14.70	14.70	0.3115	0.6264
	1.358	13.92	13.92	0.3055	0.6203

Table 4.10 The half-dimensions of the image in the x and y and the magnetic fields of the quadruplet (+ve: focus in x, defocus in y and -ve: defocus in x, focus in y) as a function of object distance calculated at various conditions. Image distance, 10cm, separation distance, 8cm and beam energy, 50 MeV.

B_1: the magnetic field setting of the outer two quadrupoles

B_2: the magnetic field setting of the inner two quadrupoles

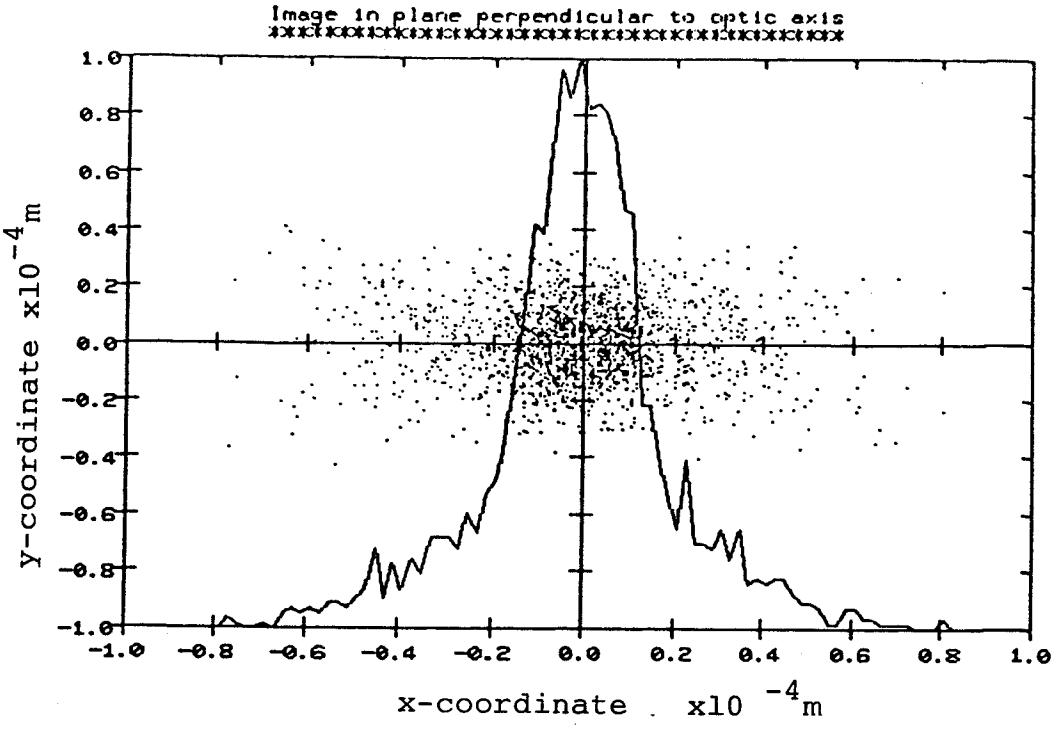

Figure 4.6 Particle distribution and integral at the image plane (10 cm) at object distance, 1.808 m, separation distance, 8 cm, θ, 5.468 mrad, ϕ, 3.62 mrad, ΔE, 0.25% and standard fringing field (2000 particles).

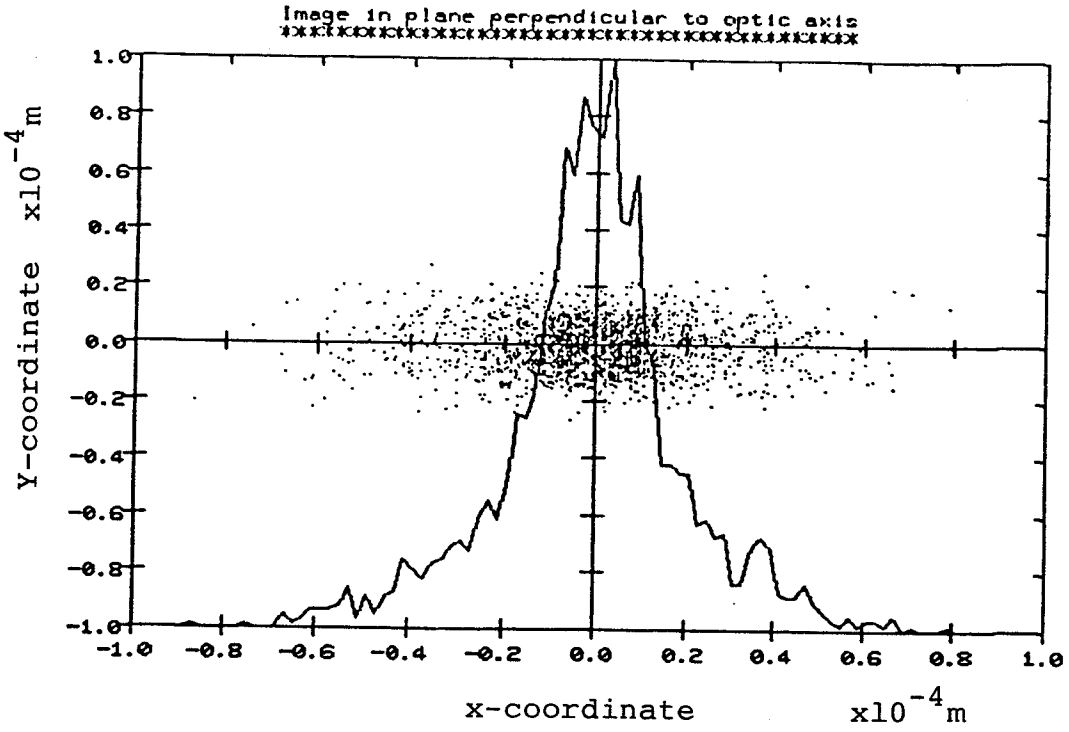

Figure 4.7 Beam distribution and integral at the image plane (10 cm) at object distance, 1.808 m, separation distance, 8 cm, θ, 5.468 mrad, ϕ, 3.62 mrad, ΔE, 0.25% and standard fringing field (2000 particles).

yz-plane as a result of minimizing the chromatic aberrations. The spherical aberrations remained unchanged.

When we tried to improve the beam current density by obtaining a smaller image from the doublet lens, the divergence angle in the yz-plane correspondingly increased. The graphic pictures of the microprobe image under these conditions are shown in figures 4.8 and 4.9. The spot size became dramatically worse due to the large aberrations, especially spherical aberrations, with the result that less than 50% of the beam is contained within the confines of the first order image. The influence is greater in the xz-plane than in the yz-plane. Hence, the dominance of spherical aberration and its contribution to enlargement of the image is clear. The effect of chromatic aberration is relatively minor and the main effort to be made is to minimize the divergence angle of the proton beam. Therefore, the design of the doublet lens had to be considered as a compromise between high current intensity and the spot size. While searching for an acceptable structure for the doublet lens, the main concern was to reduce the divergence angles of the incident beam while at the same time giving a reasonable current intensity.

The final design of the doublet, which was achieved as explained in the last section, has produced very encouraging results as shown in figures 4.10 and 4.11. The new doublet design was adopted for its advantage of improving the divergence angles in both the xz- and yz-planes as well as providing larger beam currents for the microprobe

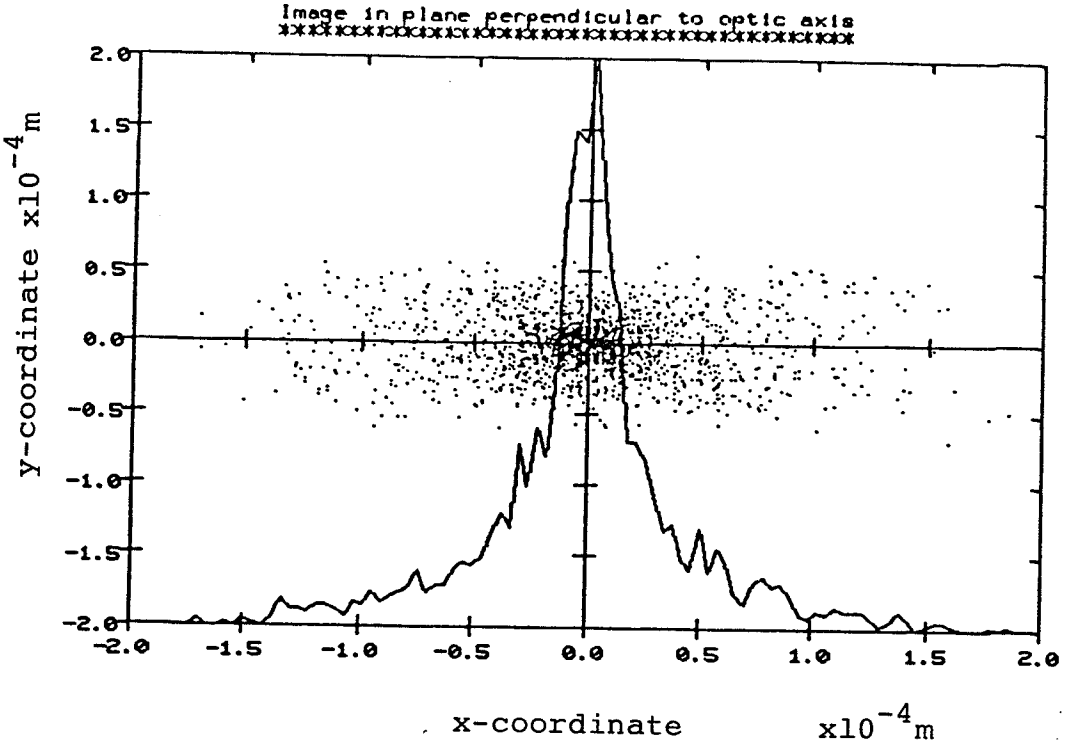

Figure 4.8 Beam distribution and integral at the image plane (10 cm) at object distance, 1.808 m, separation distance, 8 cm, θ, 5.068 mrad, ϕ, 6.606 mrad, ΔE, 0.5% and standard fringing field (2000 particles).

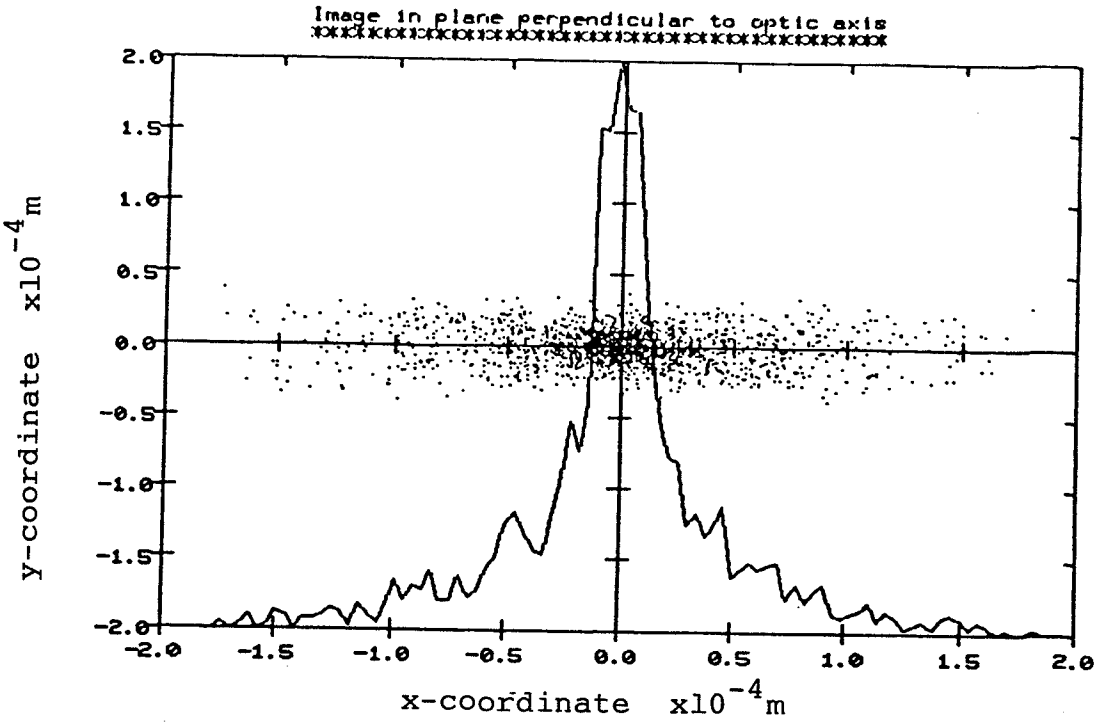

Figure 4.9 Beam distribution and integral at the image plane (10 cm) at object distance, 1.808 m, separation distance, 8 cm, θ, 5.068 mrad, ϕ, 6.606 mrad, ΔE, 0.25% and standard fringing field (2000 particles).

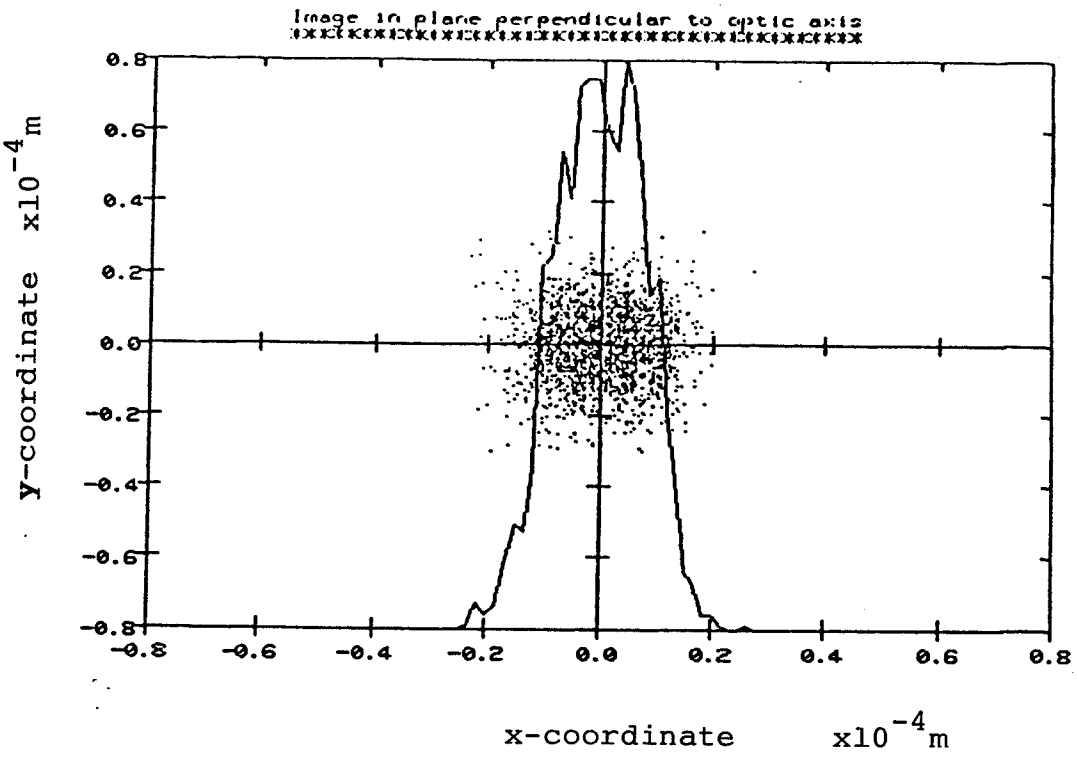

Figure 4.10 Beam distribution and integral at the image plane (10 cm) at object distance, 1.808 m, separation distance, 8 cm, θ, 2.232 mrad, ϕ, 2.5925 mrad, ΔE, 0.5% and standard fringing field (2000 particles).

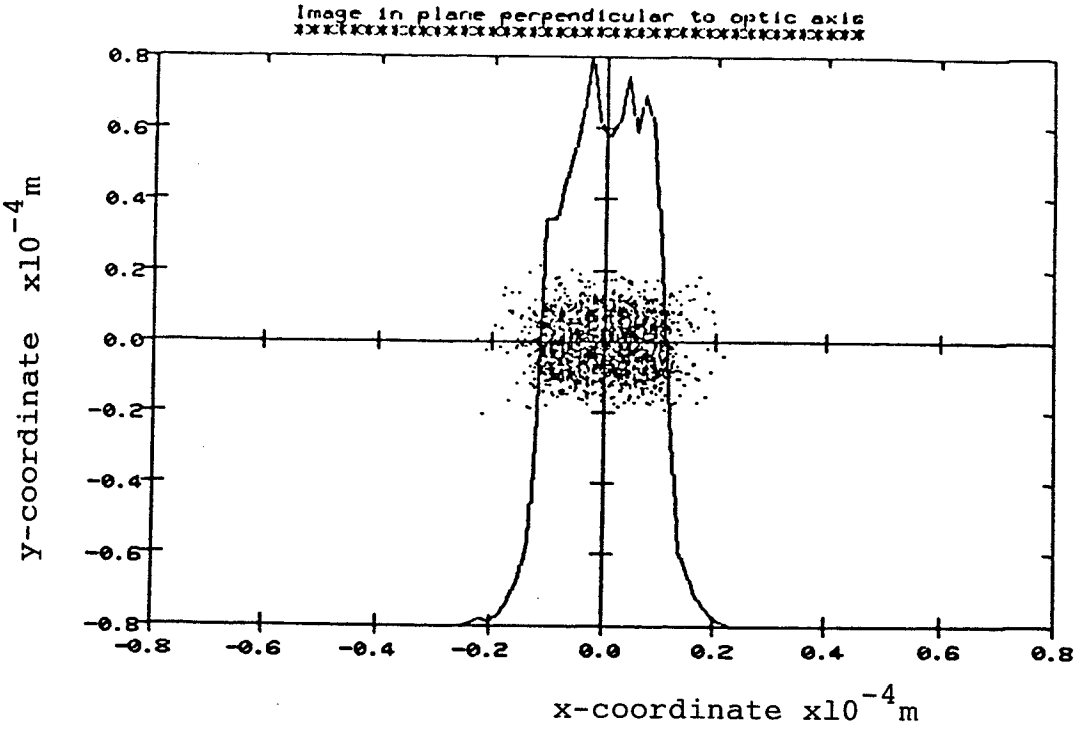

Figure 4.11 Beam distribution and integral at the image plane (10 cm) at object distance, 1.808 m, separation distance, 8 cm, θ, 2.2321 mrad, ϕ, ϕ, 2.5925 mrad, ΔE, 0.25% and standard fringing field (2000 particles).

system. As figure 4.10 shows more than 95% of the beam is now contained within the first order image and the higher order aberrations are minimal. Again the improvement in spot size stability at a smaller momentum spread (figure 4.11 as compared to figure 4.10) is obvious. The particle distribution at the image plane has proven to be independent of the beam energy.

CHAPTER 5

THE FINAL SYSTEM, CONSTRUCTION AND ASSEMBLY OF THE MICROPROBE FACILITY

CHAPTER 5

THE FINAL SYSTEM, CONSTRUCTION AND ASSEMBLY OF THE MICROPROBE FACILITY

5.1 Arrangement of the final system

In achieving the final design of our facility, the proton microprobe, a thorough analysis of the parameters of the system was necessary. Some of these considerations and constraints have already been described in previous chapters. The system will be assembled and mounted on the (15° right) beam line which is located in the experimental area of the University of Manitoba cyclotron laboratory (figure 5.1).

The proton beam coming from the cyclotron is directed by the switching magnet to the 15° right beam line and then focused by the two quadrupoles Q5 and Q6 (which are shown in figure 5.1) to form an image. At this point, we place the object slit for our doublet lens. The dimensions of the slit are 5 mm and 12 mm in the x and y directions respectively. The beam is then focused to an image of 10.08 mm and 5.6 mm in the x and y directions respectively, 5.21 m downstream. The doublet configuration has object and image distances of 2.241 m and 2.147 m. The physical length of each quadrupole, which has a square return path, is 25.08 cm and the aperture radius is 5.27 cm. The

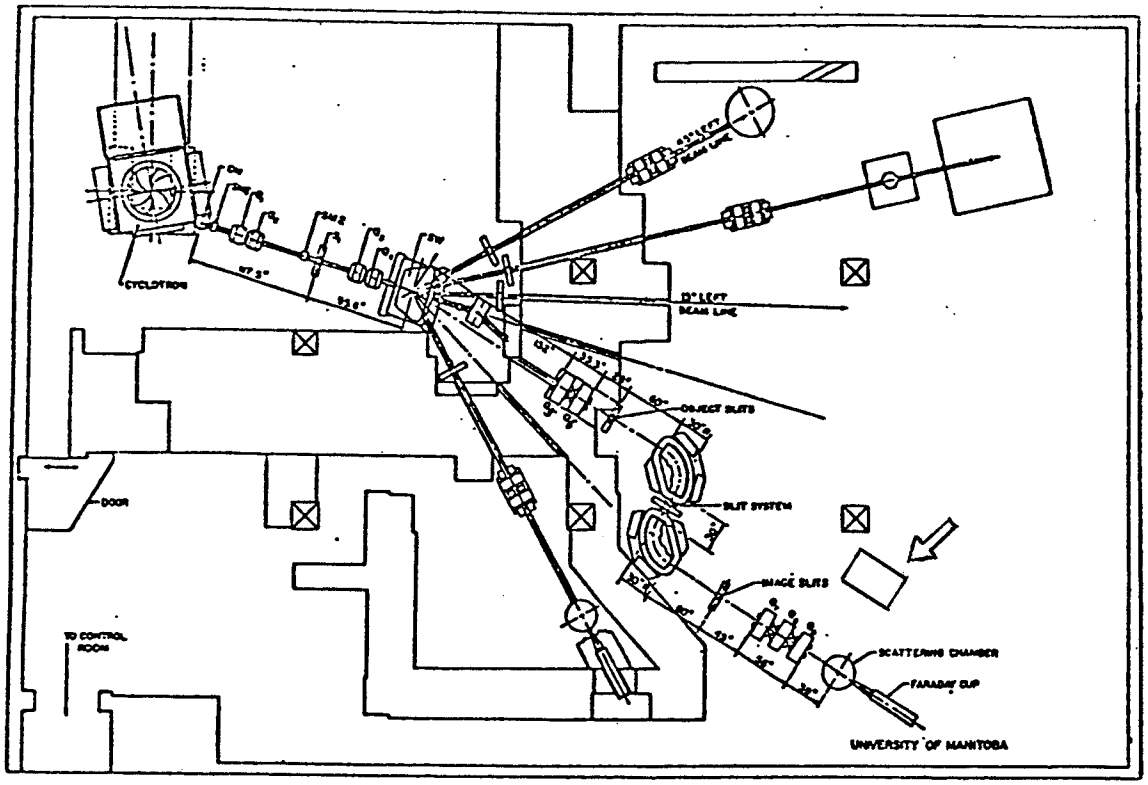

Figure 5.1 Map of the University of Manitoba Cyclotron and the experimental area. The arrow pointing at the position of the proton microprobe facility.

effective length of each of these quadrupoles is therefore 31.1 cm according to the following equation:

$$L = \ell + 1.1\ a$$

where L = effective length

ℓ = physical length

a = aperture radius

The separation distance between the two quadrupoles is equal to 20 cm and the lens is operating in CD fashion. The excitation settings are recorded in table 5.1 as a function of beam energy.

This configuration of the doublet lens will produce optimum beam parameters at the microprobe object slit position. This will provide high current densities when the beam is collimated at the object position of the microprobe system as well as the desirable low divergence angles. The object slit of the microprobe may be placed at position S (figure 5.2) which is approximately 1.405 m from the exit of the second quadrupole in the doublet system. At this place the beam is at its minimal dimension of 6.5x2 mm^2 (beam waist) and has an acceptably small divergence angle of 2.232 mrad and 2.593 mrad in the xz- and yz-planes respectively. Should higher current densities be required when the system becomes on-line, object and image distances may be adjusted by moving the doublet lens, subject to the constraint that the sum of object and image distances remains constant. The adjustment is done so that a larger object distance can be obtained at the expense of

BEAM ENERGY	B_1 (T)	$-B_2$ (T)
20	0.1731	0.1744
25	0.1938	0.1953
30	0.2126	0.2142
35	0.2300	0.2317
40	0.2461	0.2480
45	0.2614	0.2634
50	0.2759	0.2780

Table 5.1 The required magnetic field setting (+ve: focus in x, defocus in y and -ve: defocus in x, focus in y) as a function of beam energy. Object distance, 2.241m, image distance, 2.147m, separation distance, 20cm (magnetic doublet).
B_1: the magnetic field setting of the first quadrupole in the beam direction
B_2: the magnetic field setting of the second quadrupole in the beam direction

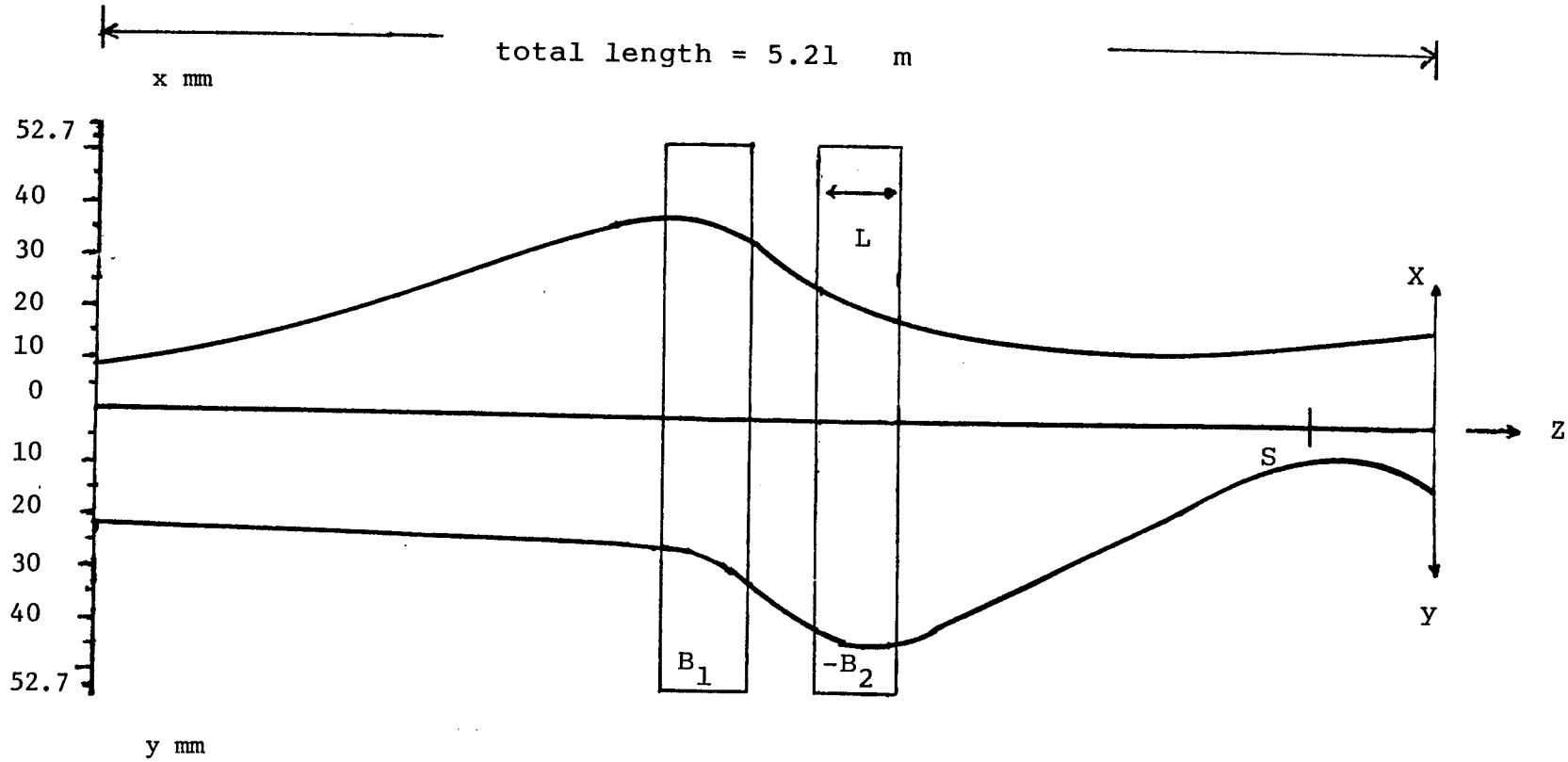

Figure 5.2 The beam envelope in the pre-microprobe magnet doublet system. The object slit for the microprobe will be located at position S in this figure.

the image distance. The values of the magnet excitation currents needed to provide focusing, change for different doublet lens locations. This adjustment produces a brighter beam spot as an object for the microprobe system for a given cyclotron beam intensity because particles previously striking the collimator now go through the aperture, as long as no alteration to the dimensions of the object slit at position S is made. However the spot size resulting from the third order aberrations increases because of the resulting larger divergence angles. If lower current density can be tolerated and smaller divergences are desirable, then this can be achieved either by decreasing the object distance of the doublet lens relative to its image distance or by including another collimator slit.

A collimator system at point S defines the object for the microprobe lens. This collimator system can be fixed at any width between 20 and 70 μm. A 70 μm slit was chosen for these calculations. The microprobe quadruplet lens is placed at a distance of 1.808 m from position S. Each of the four quadrupoles is 18.09 cm in physical length i.e. 21.15 cm effective length, and has an aperture radius of 2.7 cm. The separation distance between neighboring quadrupoles is 8 cm. The image distance is set at 10 cm from the exit of the last quadrupole. The magnetic field strengths as a function of proton energy for this system are tabulated in table 4.3. The beam envelope from the object to the image is shown in figure 5.3. The beam parameters at various positons through its journey toward the target are listed in table 5.2.

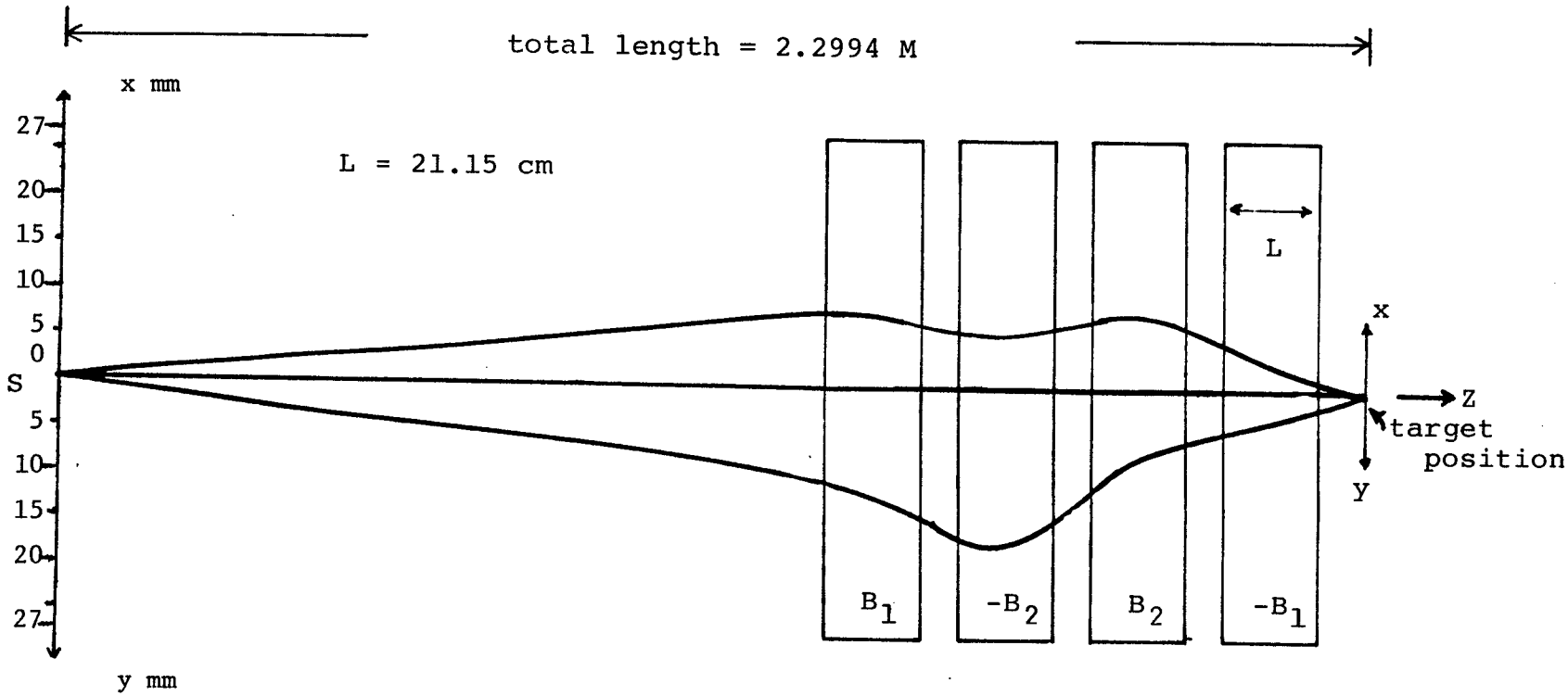

Figure 5.3 The beam envelope in the microprobe system from position S (object slit) to the image plane (target position).

POSITION	Rx	θ	Ry	Φ
At the 15° object slit for the doublet	6mm	4.5mrad	2.5mm	1.21mrad
At position S	3.25mm	2.323mrad	1mm	2.593mrad
Just after the microprobe object slit at position S	35μm	2.232mrad	35μm	2.593mrad
At the image plane of the microprobe (target position)	11.24μm	6.950mrad	11.24μm	8.074mrad

Table 5.2 Half-dimensions and half-divergence angles of the proton beam in x and y coordinates at selected positions in the final microprobe system.

The relative orientation of the quadrupoles is an essential factor since imperfect alignment can introduce major problems which lead to losing focus[21,22]. Translational alignment of the system elements can be achieved to a precision of ±26 μm. This accuracy will reduce the misalignment effect on broadening the beam. If the elements of the quadruplet are aligned mechanically, the rotational misalignment can be largely corrected by rotating one of the four quadrupoles[10]. High accuracy of adjustment in all directions is provided to all four quadrupoles. Contribution from the high order harmonic contaminations should be reduced to an acceptable level by adjusting the divergence angles as we stated earlier. The investigations indicate that the second and third order aberration coefficients are not functions of the divergence angles. Therefore, the values tabulated in table 4.10 are associated with our system and contribute to the distribution in the image plane as in figures 4.10 and 4.11. Further reduction to the spot size can be accomplished by eliminating the effects of the spherical aberrations in third order. This may be done by setting an octupole field of a certain value at the exit of the quadruplet lens[10]. Placing a slit on the image side of the lens proved of no value in eliminating the scattered particles as might have been expected. Such a slit causes a reduction in intensity as well as introducing beam scattering and background radiation[20]. The estimated current density at the target position is approximately 5 ± 0.5 pA/μm^2 per μA of cyclotron beam.

The suggested technique for scanning the sample is to move the target across the microbeam by placing it on a target holder which can be moved in both horizontal and vertical directions. This is preferable to the deflection of the microbeam across a fixed target. The latter technique has many drawbacks such as the deterioration of the quality of the beam spot.

In order to minimize the vibration effect on the microprobe system, the whole microprobe unit i.e. the object slit through to and including the target, has to be mounted on a heavy base such as a granite or honeycomb slab supported by a vibration isolation system. The system will then behave as a rigid pendulum and vibrations will be damped.

5.2 Construction and assembly of system elements

Slit edge scattering is a problem associated with all kinds of slit designs, though of varying magnitude. The scattering level has been found to be related to the slit material according to the formula $(A/\rho Z^{1/2})$ where A, ρ and Z are the atomic weight, density and atomic number of the slit material respectively[21,22], as well as the slit configuration. Collimator slits made of nickel or tantalum are favored. Four different design configurations of the collimator slits (figure 5.4) were analytically tested to minimize effects from edge scattering of the protons. These tests showed that the design suggested by Nobiling and shown in figure 5.4 (d) has the least slit scattering[2].

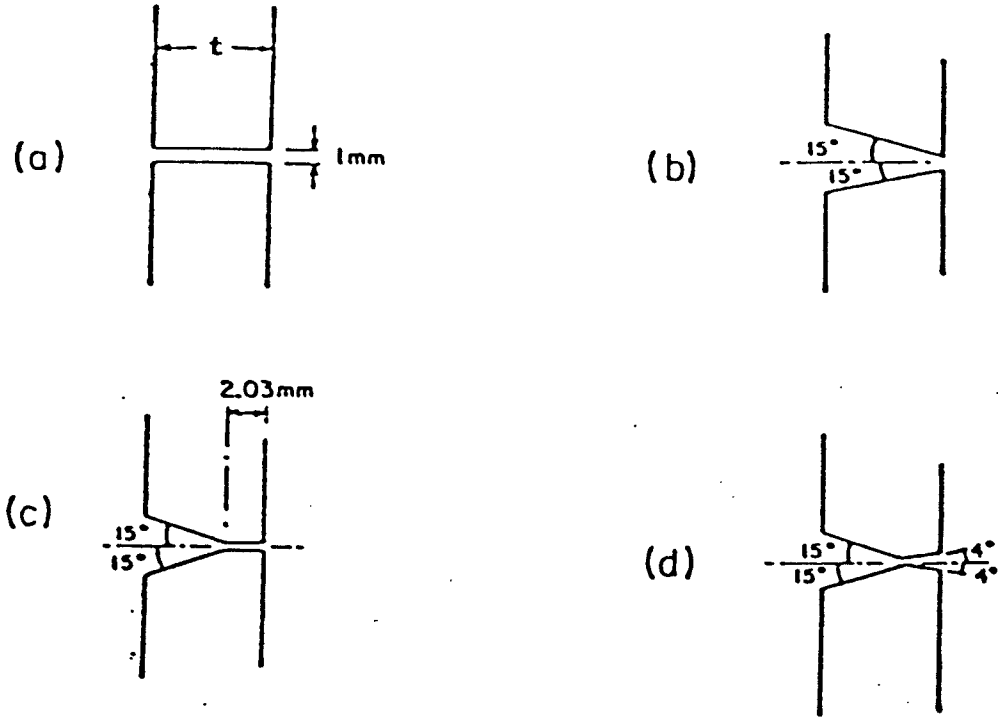

Figure 5.4 The four slit configurations tested. The thickness of the slit material (t) is identical for all the slits and is equal to the proton range (5.1 mm) at 50 MeV.

The scattering was also found to be linearly proportional to beam energy. The two sets of collimator slits, which are already assembled, are made of nickel and shaped according to Nobiling. These are water-cooled and shown in plate 5.5.

Quadrupole magnets in the doublet system are designed to have a square magnetic return path of 45.7 cm in dimension. The poles are of a circular tipped shape and tapered at the two ends to avoid saturation. A coil of 98 turns is wound around each pole. These are made up of square copper wire of 0.579 cm in dimension with a 0.325 cm square hole for water-cooling. After winding, the coils are baked in a mold with EPOXY material for 24 hours to provide rigidity to the coils. The quadrupole magnets are assembled (plate 5.6) and then mounted on V-shaped cradles which provide the adjustment required for latter lens alignment. The quadrupole doublet system is complete and has been mounted on a heavy steel table.

The microprobe quadrupoles are designed differently and with higher precision than the doublet system. This is due to the very high sensitivity of these magnets and the consequent effects on the proton microbeam. The magnetic return path is of a round shape and is 61 cm in diameter. The two ends of each pole are tapered in the same way as in the doublet magnets and the tips are carefully rounded with very high precision to minimize the surface roughness of the pole tips in order to ensure uniformity in the magnetic field distribution as well as minimizing parasitic aberrations. A squared-shaped coil of 56 turns is

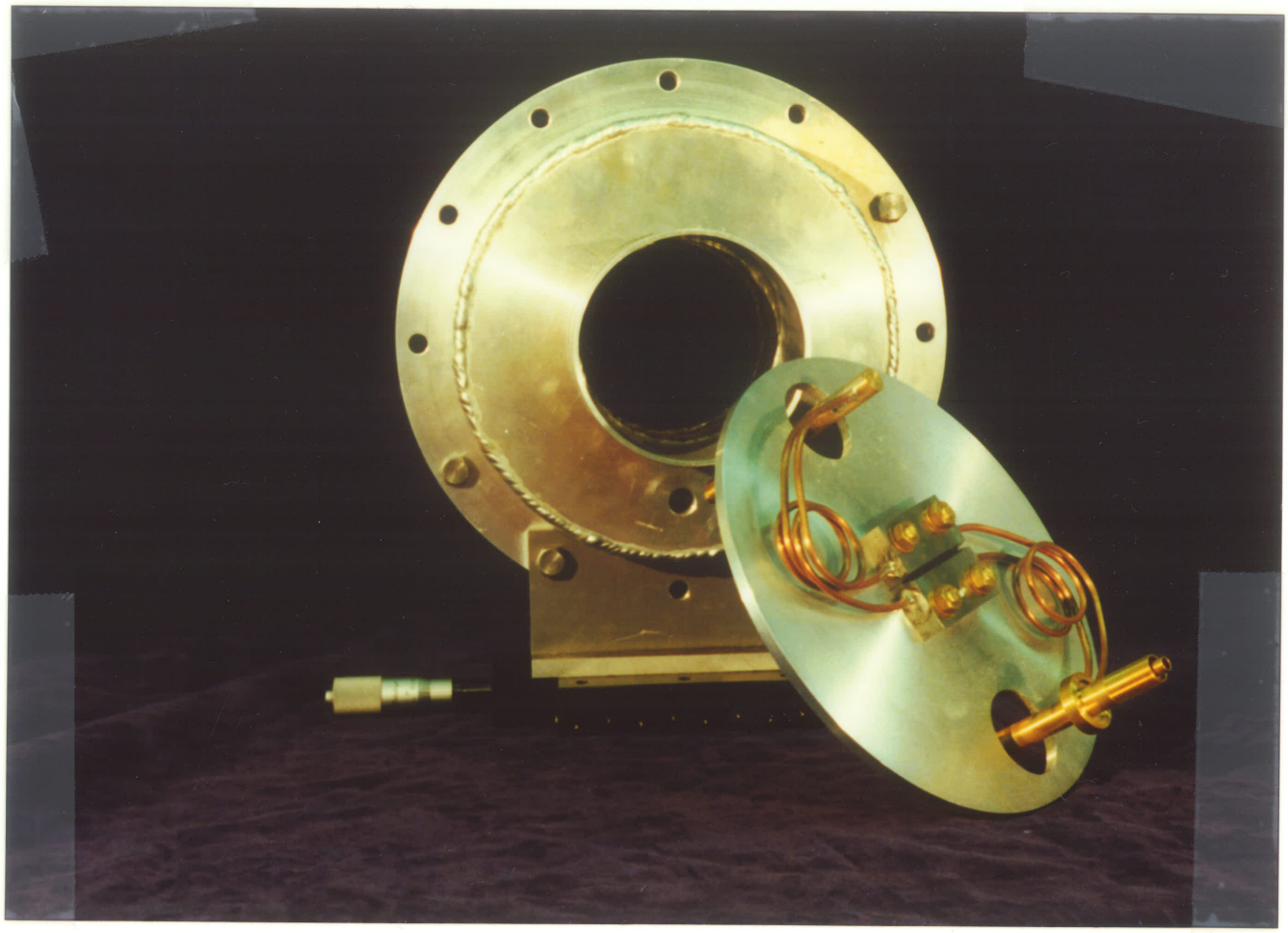

Plate 5.5 The collimator slit system which was built in the Faculty of Science Mechanical Workshop.

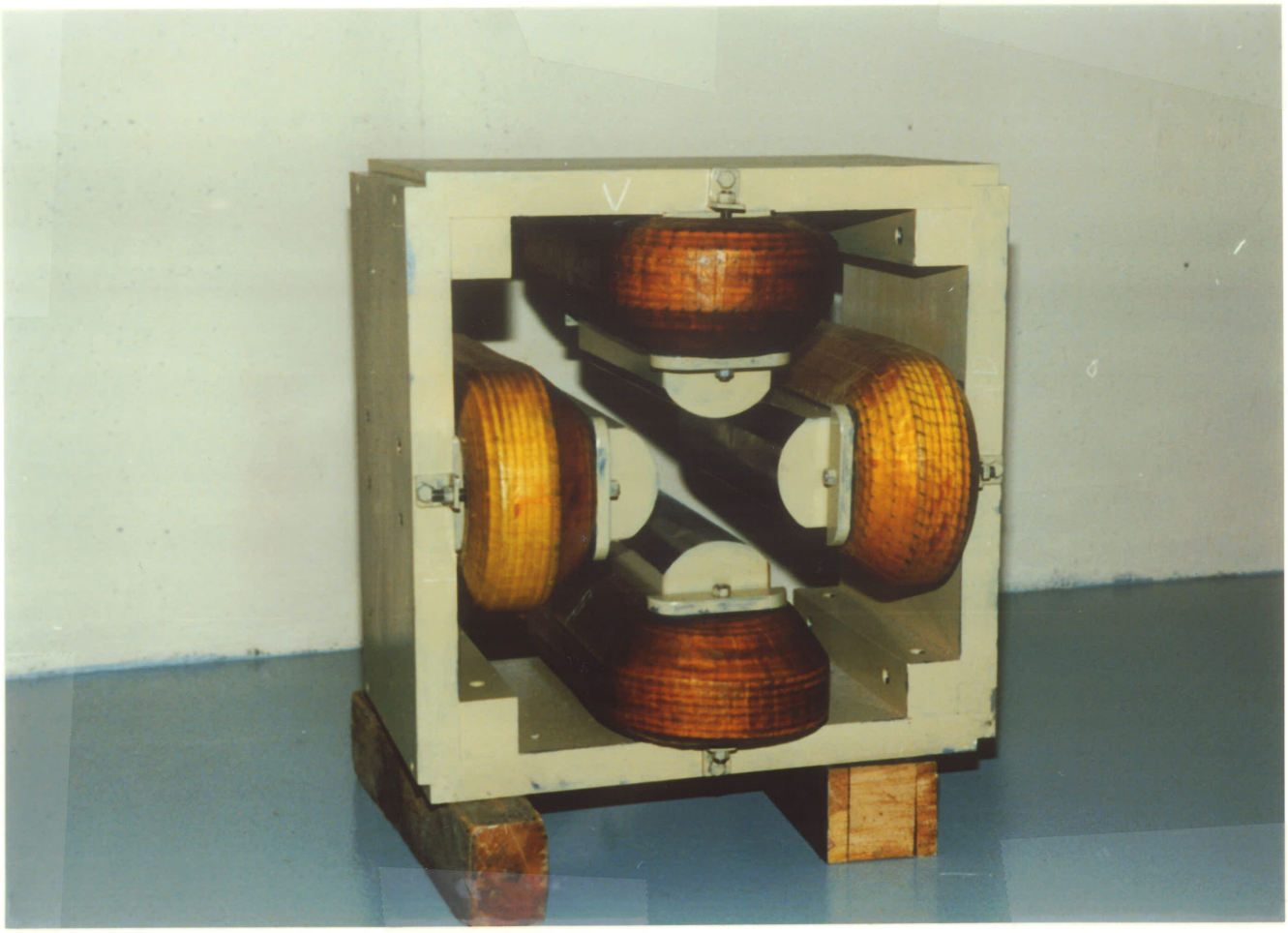

Plate 5.6 One of the two magnetic quadrupoles of the doublet system.

wound around each pole. Again, these coils are made up of the same type of copper wire as in the doublet system. For the purpose of providing high rigidity, these coils are placed into a mold where they are vacuum impregnated using a special type of EPOXY. The high excitation currents which are supplied to these coils cause the coils to attract one another upon excitation. Currently, the four microprobe magnets have already been constructed in our magnet workshop, and are ready to be assembled into a unit.

Plate 5.7 illustrates one of these quadrupole magnets before assembly. A prototype magnet was built for a magnetic field distribution tests earlier and the results were satisfactory as has been described earlier in chapter (4). Since the multidirectional alignment of the microprobe quadrupoles is very critical and required a precision of 100 μm, specially designed cradles were built to accommodate these magnets. This design, which is illustrated in plate 5.8, will provide an alignemt in x, y and z directions with a precision of 26 μm.

At this stage, extent of the effect of vibration on the system is not known. Therefore, to minimize the total costs, a rather cheap heavy steel table made of available material has been built to hold the microprobe unit. Should the vibration effects be found to be very destructive to the microbeam, the steel table may be replaced by granite or honeycomb with vibration free isolation.

Plate 5.7 One of the microprobe quadrupole magnets before assembly. The figure shows the return path, a pole piece and one of the vacuum impregnated coils.

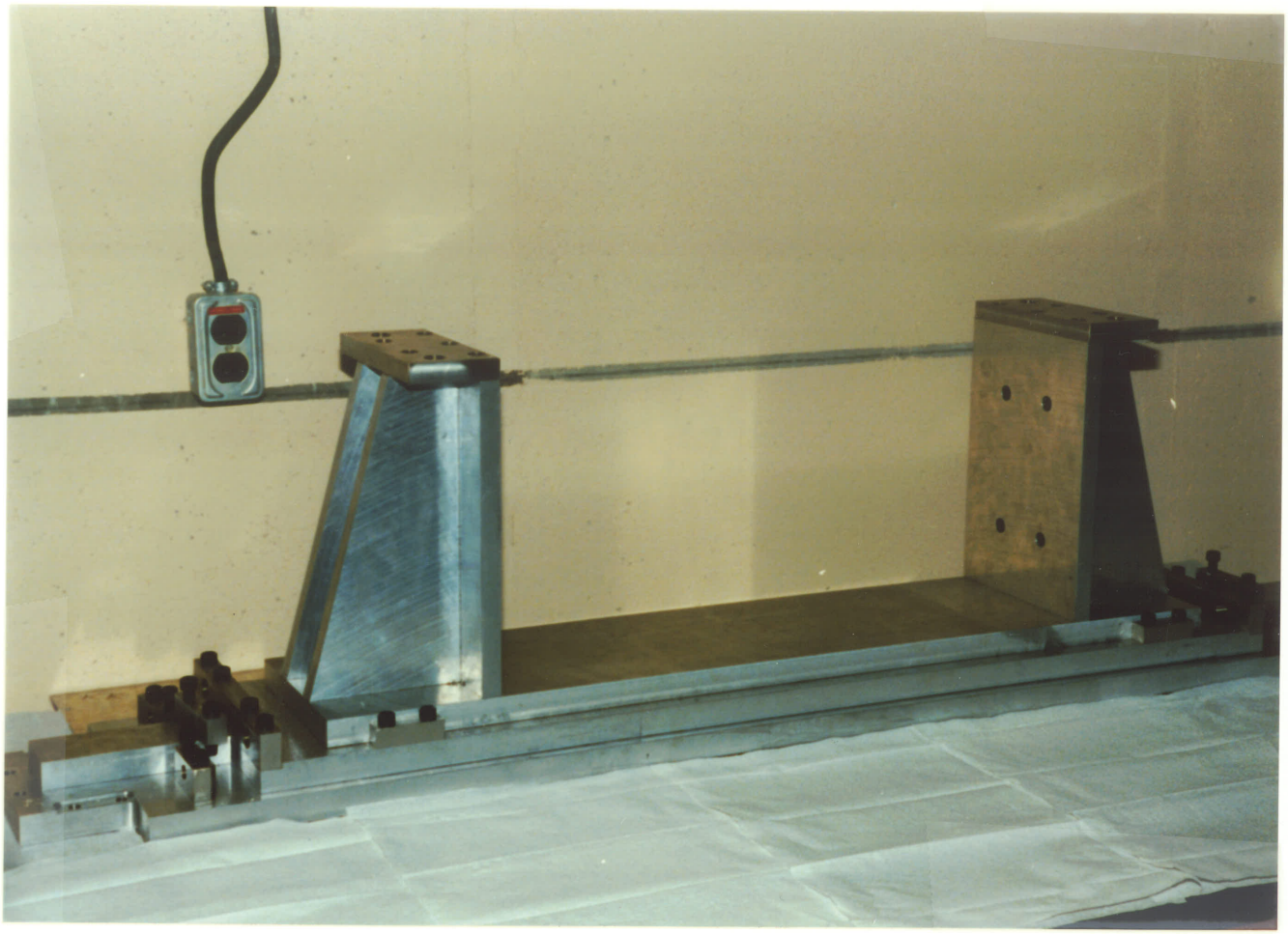

Plate 5.8 The specially designed high sensitivity adjustment cradle for the microprobe quadrupole magnets.

Since the expertise is available, the construction of all the elements described in this text has been carried out at the magnet and machine workshops of the Faculty of Science, University of Manitoba. The copper coils were wound, insulated and their resistance was tested for continuity. Another test was performed on the vacuum-impregnated coils to examine the effects of operating at high magnitization currents. A coil was loaded by currents of up to 150 amperes for 24 hours with full water-cooling. No overheating or cracking was noticed.

CHAPTER 6

CONCLUSIONS AND FINAL REMARKS

CHAPTER 6

CONCLUSION AND FINAL REMAKRS

The results from this study of beam parameters and ion optics of the University of Manitoba microprobe system can be summarized as follows:

1. The separation distance between neighboring quadrupole magnets must be kept as small as possible, within mechanical limitations, so as to minimize image spot size. The physical lmitations set by our magnet windings require that the smallest achievable separation distance is 8 cm.

2. The image size and the quadrupole fields are inversely proportional to object distance, for a constant image distance. Using very long object distances, which will minimize image size, introduces several disadvantages:

   (a) The need for high stability power supplies for magnets ($\Delta I/I = 10^{-5}$ to 10^{-8}).

   (b) The need for excessive space to contain the microprobe.

   (c) The problems associated with the effect of stray external fields on beam stability.

The 1.808 m object distance which was chosen produces a spot size of 22.5 x 22.5 μm^2, at an image distance 10 cm from the exit of the microprobe. The assumed object size was 70x70 μm^2. For a smaller object size the achievable image spot size will be reduced by the same ratio. The current intensity in the image becomes correspondingly smaller. Finally, this image spot size can be further decreased if the beam emittance is improved or if more space becomes available.

3. At a fixed object distance, the image size is linearly proportional to image distance while the magnetic fields are again inversely proportional to image distance.

   Chromatic and spherical aberration coefficients in second and third order are found to be independent of beam energy or divergences. These aberration coefficients do depend, however, on the image and object distances as described in chapter (4).

4. Chromatic and spherical aberration coefficients change noticeably when a fringing field is included in the beam optics calculation. The shape of the fringing field, however, has negligible effect on the values of these coefficients.

5. The divergence of the incident beam contributes significantly to the third order spherical aberrations in the spot size. These aberrations dominate over second order chromatic aberrations. Thus,

more emphasis must be placed on the minimization of spherical aberrations.

The Nobiling design for collimator slits was adopted in order to minimize slit edge scattering of protons.

A careful procedure for aligning the quadrupole magnets at assembly will be necessary.

Possible improvement in the microprobe system

In order to further reduce spherical and chromatic aberrations, additional beam optical studies could be useful.

Should the microbeam current be inadequate to produce sufficient x-ray intensity from a target, the doublet system can be adjusted with respect to the object and image planes, thus increasing the object distance relative to the image distance. This increases the brightness of the object for the microprobe system as described in chapter (5).

Smaller divergence angles can be obtained, either by reducing the ratio of the object to image distance of the upstream doublet or by mounting a collimator slit at a certain distance from the object slit of the microprobe. These two effects are interdependent, but an optimum condition can be found.

Finally, the microbeam image can be studied in detail by observing the spot size on a scintillating material with an optical microscope.

REFERENCES

1. F. W. Martin, presentation to the symposium of Northeastern Accelerator Personnel, Stony Brook, N.Y., Oct. 15, 1984.

2. Ravi Prakash, M.Sc. Thesis, 1985.

3. J. A. Cookson, A.T.G. Ferguson and F.D. Pilling, Journal of Radioanalytical Chemistry, 12, 39, 1972.

4. F. Watt, G.W. Grime, G.D. Blower and J. Takacs, IEEE Trans. on Nucl. Sci., NS-28, No.2, 1413, 1981.

5. J. A. Cookson, Nucl. Instr. and Meth., 165, 477, 1979.

6. F.W. Martin and R. Goloskie, Presentation at the 4th Inter. Conf. on Proton-Induced X-Ray Emission, Tallanassee, Fla., June 9-13, 1986.

7. T. B. Johansson, R. A. Akselsson and S. A. E. Johansson, Nucl. Instr. and Meth., 84, 141, 1970.

8. B. Martin and R. Nobiling, Advances in Electronics and Electron Physics, Supplement 13A, 321, 1980.

9. W. D. Ramsay, M. S. A. L. Al-Ghazi, J. Birchall and J. S. C. McKee, Physics Letters, 69A, No.4, 258, 1978.

10. G. W. Grime and F. Watt, "Beam Optics of Quadrupole Probe-Forming Systems", Adam Hilger Limited, 1984.

11. C. J. Maggiore, Scanning Electron Microscopy, I, 439, 1980.

12. G. J. F. Legge, Nucl. Instr. and Meth., 197, 243, 1982.

13. F. Bosch, A. El Goresy, B. Martin, B. Povh, R. Nobiling, D. Schwalm and K. Traxel, Nucl. Instr. and Meth., 149, 665, 1978.

14. H. Kneis, B. Martin, R. Nobiling, B. Povh and K. Traxel, Nucl. Instr. and Meth., 197, 79, 1982.

15. R. Nobiling and K. Traxel, Nucl. Instr. and Meth., 142, 49, 1977.

16. W. Bischof, M. Hofert, H. R. Wilde, B. Raith and B. Gonsoir, Nucl. Instr. and Meth., 197, 201, 1982.

17. H. R. Wilde, W. Bischof, B. Raith, C. D. Uhlhorn and B. Gonsoir, Nucl. Instr. and Meth., 181, 165, 1981.

18. R. Prakash and J. S. C. McKee, Nucl. Instr. and Meth., B 1011, 679, 1985.

19. J. C. den Ouden, A. J. J. Bos, R. D. Vis and H. Verheul, Nucl. Instr. and Meth., 181, 131, 1981.

20. H. Bruckmann, W. Vogel, H. W. Boie and U. Schroder, 9th Inter. Conf. on Cycl. and their Appl., 719, 1981.

21. M. S. A. L. Al-Ghazi, Ph.D. Thesis, 1983.

22. M. S. A. L. Al-Ghazi and J. S. C. McKee, Nucl. Instr. and Meth., 197, 117, 1982.

23. P. W. Hawkes, "Quadrupoles in Electron Lens Design", Advance in Electronics and Electron Physics, Academic Press, 1970.

24. A. D. Dymnikov, T. Ya. Fishkova and S. Ya. Yavor, Soviet Physics - Technical Physics, 10, No.3, 340, 1965.

25. A. Septier, "Focusing of Charged Particles", I, Academic Press, 1967.

26. W. G. Davies, "Introduction to First Order Optics", Two Lectures given to SCANDITRONIX Staff, Chalk River Nuclear Laboratories, Atomic Energy of Canada Limited, May 1982.

27. A. P. Banford, "The Transport of Charged Particle Beams", E. & F. N. Spon Limited, London, 1966.

28. Ulf Lindh and Torbjorn Sude, Nucl. Instr. and Meth., B10/11, 703, 1985.